Contributions to Mineralogy and Petrology _###################_
https://doi.org/10.1007/s00410-019-1640-0

ORIGINAL PAPER

Origin of pyroxenites in the oceanic mantle and their implications on the reactive percolation of depleted melts

V. Basch[1] · **Elisabetta Rampone**[1] · **G. Borghini**[2] · **C. Ferrando**[3] · **A. Zanetti**[4]

Received: 8 July 2019 / Accepted: 25 October 2019
© Springer-Verlag GmbH Germany, part of Springer Nature 2019

Abstract

Pyroxenites are diffuse in fertile mantle peridotites and considered an important component in the mantle source of oceanic basalts. They are rarely documented in abyssal and ophiolitic peridotites representing residual mantle after melt generation, and few studies defining their origin are to date available. We present a field-based microstructural and geochemical investigation of the pyroxenite layers associated with depleted peridotites from the Mt. Maggiore ophiolitic body (Corsica, France). Field and petrographic evidence indicate that pyroxenite formation preceded the melt–rock interaction history that affected this mantle sector during Jurassic exhumation, namely (1) spinel-facies reactive porous flow leading to partial dissolution of the pyroxenites, and (2) plagioclase-facies melt impregnation leading to [plagioclase + orthopyroxene] interstitial crystallization. Pyroxenes show major element compositions similar to abyssal pyroxenites from slow-spreading ridges, indicative of magmatic segregation at pressures higher than 7 kbar. Both the parental melts of pyroxenites and the melts involved in the subsequent percolation were characterized by Na_2O-poor, LREE-depleted compositions, consistent with unaggregated melt increments. This implies that they represent the continuous evolution of similarly depleted melts leading to different processes (pyroxenite segregation and later melt–rock interaction) during their upward migration. To support the genetic relation and the continuity between the formation of pyroxenites and the subsequent melt–rock interaction history, we modeled all the documented processes in sequence, i.e.: (1) formation of single-melt increments after 6% mantle decompressional fractional melting; (2) high-pressure segregation of pyroxenites; (iii) spinel-facies reactive porous flow, (4) plagioclase-facies melt impregnation. The early fractionation of pyroxenites leads to a decrease in pyroxene saturation that is necessary for the subsequent reactive porous flow process, without any significant change in the melt REE composition.

Keywords Pyroxenite · Melt–rock interaction · Mantle melting · pMELTS · Oceanic lithosphere · Alpine ophiolite

Introduction

Pyroxenite bodies and/or layers are a minor but diffuse lithotype in fertile mantle peridotites and are considered an important component in the mantle source of oceanic basalts (e.g. Hirschmann and Stolper 1996; Stracke et al. 1999; Salters and Dick 2002; Kogiso et al. 2004a, b; Sobolev et al. 2005, 2007; Lambart et al. 2013, 2016; Borghini et al. 2017). However, their origin remains a debated issue, since various magmatic and metamorphic processes can be invoked: (1) metamorphic recycling of subducted oceanic crust incorporated into the lithosphere (e.g. Allègre and Turcotte 1986; Morishita and Arai 2001; Morishita et al. 2003; Yu et al. 2010); (2) reactive melt percolation and "refertilization" of a depleted upper mantle during melt–peridotite interactions (Garrido and Bodinier 1999; Bodinier et al. 2008; Dantas et al. 2009; van Acken et al. 2010; Laukert et al. 2014;

Communicated by Othmar Müntener.

Electronic supplementary material The online version of this article (https://doi.org/10.1007/s00410-019-1640-0) contains supplementary material, which is available to authorized users.

✉ Elisabetta Rampone
betta@dipteris.unige.it

[1] Dipartimento di Scienze della Terra, dell'Ambiente e della Vita (DISTAV), Università degli Studi di Genova, Corso Europa 26, 16132 Genoa, Italy

[2] Dipartimento di Scienze della Terra "Ardito Desio", University of Milano, Milan, Italy

[3] CRPG, University of Lorraine, Nancy, France

[4] CNR-IGG, Sezione di Pavia, Pavia, Italy

Borghini et al. 2013, 2016); (3) moderate-to-high-pressure melt segregation derived from asthenospheric melting (Bodinier et al. 1987a, b; Vannucci et al. 1993; Rivalenti et al. 1995; Kempton and Stephens 1997; Mukasa and Shervais 1999; Takazawa et al. 1999; Dantas et al. 2007; Keshav et al. 2007; Warren et al. 2009; Gysi et al. 2011).

Pyroxenites are commonly documented in association with fertile peridotites but only few studies have investigated pyroxenite layers and veins associated with depleted oceanic and ophiolitic peridotites representing residual mantle after partial melting of asthenospheric sources (e.g. Dantas et al. 2007; Warren et al. 2009; Laukert et al. 2014). These studies in oceanic settings inferred an origin of the pyroxenite layers as deep-seated (spinel-facies) magmatic segregations of depleted unaggregated melts and/or as replacive lithotypes after melt–rock interactions. Melt–rock interactions are increasingly invoked in extensional settings as key processes in modifying the modal and chemical composition of the host rock (lithospheric mantle and/or lower oceanic crust) and percolating melt (e.g. Collier and Kelemen 2010; Paquet et al. 2016; Rampone et al. 2016, 2019; Sanfilippo et al. 2016; Basch et al. 2018, 2019; Borghini et al. 2018; Ferrando et al. 2018; McCarthy and Muntener 2019). Therefore, the understanding of the origin of pyroxenites associated with residual peridotites and deciphering the melt–rock interaction processes is of utmost importance to constrain processes of melt production in oceanic environments, as well as the chemical evolution of melts during percolation through the oceanic lithosphere.

In the Mt. Maggiore ultramafic massif (Alpine Corsica, France), partially dissolved pyroxenite layers are associated with residual mantle peridotites that record a complex melt–rock interaction history from spinel-facies to plagioclase-facies conditions (Rampone et al. 1997, 2008; Müntener and Piccardo 2003; Piccardo and Guarnieri 2010; Basch 2018; Basch et al. 2018). Field evidence clearly indicates that pyroxenites preceded the latter melt migration stages. Previous geochemical studies (Rampone et al. 1997, 2008; Piccardo and Guarnieri 2010; Basch et al. 2018) documented that melts involved in the reactive percolation process have depleted compositions and likely represent last melt increments formed at the top of a mantle column after 5–8% fractional melting of a Depleted MORB Mantle source (DMM). The percolation of depleted melts in the oceanic lithosphere has been extensively reported in slow-spreading oceanic setting, both in ophiolites (Rampone et al. 1997, 2008, 2019; Dijkstra et al. 2003; Piccardo et al. 2007; Rampone and Borghini 2008; Sanfilippo and Tribuzio 2011; Basch et al. 2018) and in modern mid-ocean ridges (Dantas et al. 2007; Dick et al. 2010; Warren and Shimizu 2010; Laukert et al. 2014). These peculiar melt compositions have been invoked as parental melts to pyroxenite layers from South-West Indian Ridge and Lena Trough (Dantas et al. 2007; Laukert et al. 2014). Records of depleted melts are mostly found in such relatively cold oceanic environments, as a result of a thick thermal boundary layer (TBL) and low melt production (e.g. Langmuir and Forsyth, 2007; Rampone et al. 2019) that does not allow for melt aggregation before extraction. Their composition and origin as unaggregated increments of fractional mantle melting has been well defined and modeled in terms of trace elements (e.g. Rampone et al. 2008; Basch et al. 2018) but little is known about their major element composition.

In this paper, we investigate the formation process of the Mt. Maggiore pyroxenite layers and its impact on the compositional evolution of percolating melts and the melt–rock interaction history. We used a multi-disciplinary approach combining field observations, microstructural and mineral major and trace element analyses. Our results were integrated with the melt–rock interaction history previously described in the host peridotites. Major outcomes of this study are: (1) the formation of the pyroxenites as early segregates from unaggregated depleted melts; (2) the necessity of pyroxene fractionation prior to the documented melt–rock interaction history; (3) the demonstration of the evolution of reactive processes and chemical composition of depleted melts during upward migration in a thick TBL.

Structural and petrologic background

The Corsican peridotitic bodies are part of the Alpine-Apennine ophiolites, interpreted as the oceanic lithosphere remnants of the narrow Jurassic Ligurian Tethys basin. It was opened by passive lithosphere extension and ultimately led to slow- to ultra-slow spreading oceanization (20 mm/year; e.g. Rampone et al. 2014). The Mt. Maggiore peridotitic massif is thought to represent the base of the reconstructed "Schistes Lustrés" ophiolitic sequence exposed in the eastern Alpine Corsica (Jackson and Ohnenstetter 1981). Although it lacks any crustal cover, it preserves clear field relationships between mantle peridotites and associated pyroxenite and gabbroic intrusions. Previous geochemical studies demonstrated that clinopyroxenes in clinopyroxene-poor spinel lherzolites have relatively homogeneous LREE-depleted trace element compositions, consistent with residual mantle after low degrees (5–8%) of fractional melting (Rampone et al. 1997, 2008). The peridotitic body also records a subsequent multi-stage lithospheric exhumation history, through various episodes of melt–rock interaction from deep (spinel-facies) to shallower mantle depths (plagioclase-facies) (Müntener and Piccardo 2003; Piccardo and Guarnieri 2010; Rampone et al. 1997, 2008; Basch et al. 2018).

A first event of olivine-saturated reactive melt percolation led to the dissolution of clinopyroxene and orthopyroxene, and crystallization of olivine at spinel-facies conditions. This melt–rock interaction is mostly recorded in reactive clinopyroxene-poor lherzolites and harzburgites by the development of olivine embayments partly replacing mantle orthopyroxene and clinopyroxene. Extensive reactive melt percolation led to the replacive formation of spinel dunite pods (e.g. Basch et al. 2018) and partial to complete dissolution of associated pyroxenite layers (Piccardo and Guarnieri 2010).

Plagioclase-bearing peridotites and troctolites show microstructural characteristics indicative of a plagioclase-(± opx) crystallizing, olivine-dissolving melt impregnation (Rampone et al. 1997, 2008; Müntener and Piccardo 2003; Piccardo and Guarnieri 2010; Basch et al. 2018). Highly impregnated plagioclase peridotites often display plagioclase-rich gabbronoritic veinlets, crystallized after segregation of the percolating melts. Rock-forming minerals in the gabbronoritic veinlets (plagioclase, orthopyroxene and clinopyroxene) show LREE-depleted patterns, indicating a depleted composition of the impregnating melts. This melt composition has been previously described as consistent with depleted single melt (unaggregated) increments, formed after 5–8% of mantle fractional melting (Rampone et al. 1997, 2008; Basch et al. 2018), not corresponding to classical aggregated MORBs.

Together, the reported melt–rock interaction processes suggest open-system reactive percolation of olivine-saturated depleted melts at spinel-facies levels, followed by impregnation of the peridotites by depleted melts at shallower, colder lithospheric depths. Rampone et al. (2008) and Basch et al. (2018) described the progressive modification of the composition of percolating melt during upward migration. They inferred that melt–rock interaction occurring at spinel-facies led to a progressive decrease in the olivine saturation and increase in pyroxene and plagioclase saturation. Therefore, the reaction-driven variation of the melt composition, together with the changes in pressure–temperature conditions, enabled an evolution in the type of melt–rock interaction from an olivine-crystallizing, pyroxene-dissolving reactive melt percolation at spinel-facies to a plagioclase + orthopyroxene ± clinopyroxene melt impregnation at plagioclase-facies. This implies a continuity in the documented multi-stage melt–rock interaction history, tracking progressive exhumation of this mantle sector (Basch et al. 2018). Both spinel and plagioclase peridotites were intruded by later gabbroic dykes, ranging from olivine gabbros to diorites, showing MORB-type affinity (Piccardo and Guarnieri 2010).

Field relationships and sampling

The Mt. Maggiore peridotitic massif (Corsica, France) is mainly composed of granular spinel and plagioclase peridotites, showing in places a weak NW–SE foliation marked by a preferential elongation of mantle pyroxenes (see Fig. 1 in Basch et al. 2018). The spinel peridotites show variations in modal compositions, ranging from clinopyroxene-poor lherzolites to olivine-rich harzburgites (up to 85 vol % olivine). In places, the spinel peridotites show diffuse to sharp contacts with metre-size spinel dunitic bodies. Mantle peridotites are associated with decimetre-size spinel pyroxenite layers (Fig. 1a) showing a constant NW–SE orientation throughout the ultramafic body, similar to the peridotite foliation (see Fig. 1 in Basch et al. 2018). In places, spinel pyroxenite layers show variable amounts of pyroxene dissolution (Fig. 1b–d) and replacement by interstitial olivine (Fig. 1b, d), as previously documented in the host peridotites during their reactive transformation from clinopyroxene-poor lherzolite to harzburgite and replacive dunite (Basch et al. 2018). Within the dunite, the occurrence of aligned spinel trails also suggests the former presence of a pyroxenite layer, in which pyroxenes were completely dissolved during the spinel-facies reactive porous flow (Piccardo and Guarnieri 2010; Basch et al. 2018).

A recent study of the Mt. Maggiore peridotitic massif documented the presence of an impregnation front (Basch et al. 2018) in the field. The latter marks the transition from spinel peridotites and associated spinel pyroxenite layers to plagioclase-bearing peridotites and pyroxenites, showing enrichments in interstitial plagioclase and orthopyroxene (Fig. 1d, e). The most impregnated peridotites (up to 30 vol % interstitial plagioclase + orthopyroxene) show a steeply dipping (50°–70°S) ESE–WNW modal layering of plagioclase enrichment and associated gabbronoritic veinlets crosscutting the peridotite foliation and pyroxenite layers (Rampone et al. 2008, 2019; Piccardo and Guarnieri 2010; Basch et al. 2018). All spinel- and plagioclase-bearing lithotypes are crosscut by steeply dipping gabbroic dikes (60°–80°S), trending E–W to ESE–WNW.

Sampling and analytical methods

We sampled eight pyroxenite layers, associated with both spinel and plagioclase peridotites (Table 1). These pyroxenites are characterized by variable extents of pyroxene dissolution (Fig. 1b, c; Table 1) and plagioclase-bearing impregnation (Fig. 1d, e). Although spinel pyroxenites (M11-6, M11-7, M11-7B, M11-8; associated with spinel peridotites; Fig. 1a, b) showed no sign of impregnation on the field, they all bear microstructural evidence of minor interstitial plagioclase and orthopyroxene (Fig. 1d, e; Table 1). Plagioclase pyroxenites (M11-4C, M11-5B, M11-12A, M11-12C; associated with plagioclase peridotites; Fig. 1d, e) show stronger enrichments in impregnation-related phases (plagioclase up to 15 vol%).

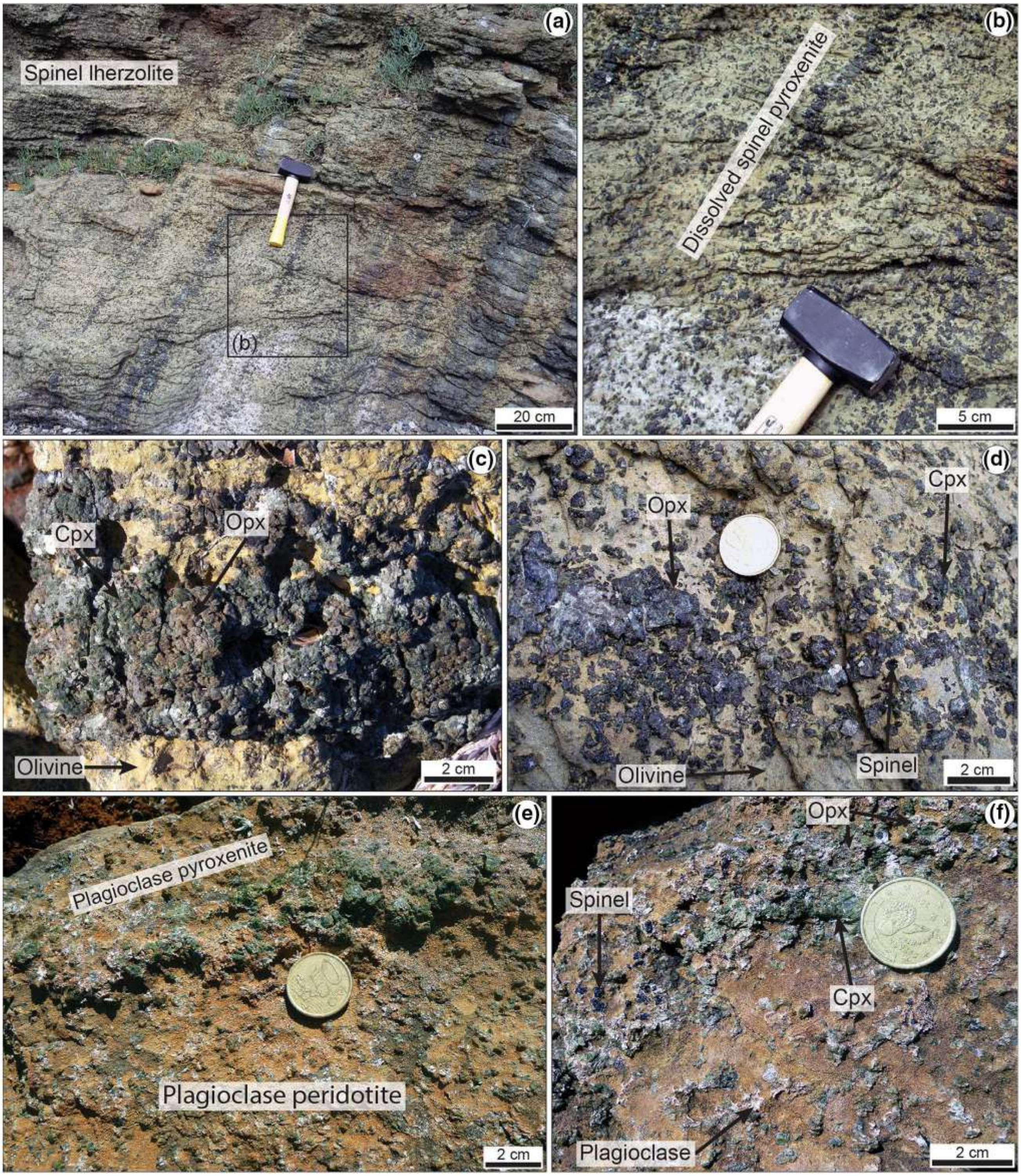
(a)
Spinel lherzolite
(b)
20 cm
(b)
Dissolved spinel pyroxenite
5 cm
(c)
Cpx
Opx
Olivine
2 cm
(d)
Opx
Cpx
Olivine
Spinel
2 cm
(e)
Plagioclase pyroxenite
Plagioclase peridotite
2 cm
(f)
Opx
Spinel
Cpx
Plagioclase
2 cm

Fig. 1 Representative field occurrences of pyroxenite layers within the Mt. Maggiore peridotitic body. **a** Partially dissolved pyroxenite layers within country spinel lherzolite; **b** partially dissolved spinel pyroxenite; **c** close-up of one of the least dissolved spinel websterite. *Cpx* clinopyroxene, *Opx* orthopyroxene; **d** close-up of a partially dissolved spinel websterite; **e** plagioclase pyroxenite within country impregnated peridotite; **f** close-up of a plagioclase pyroxenite, showing interstitial plagioclase and orthopyroxene enrichments

Table 1 Studied samples, lithotype (based on field relationship with host peridotite), modal composition, BA-index, grain number, and PfJ olivine

Sample	Lithotype	Modal compositions (vol%)					EBSD data				
		Ol	Cpx	Opx	Plagio	Sp	BA-index	*N*°	PfJ [100]	PfJ [010]	PfJ [001]
M11-7B	Sp. pyroxenite	20	35	40	5	0	0.432	43	2.03	2.25	2.10
M11-4C	Pl. pyroxenite	20	25	45	10	0	0.428	42	1.43	1.81	1.72
M11-5B	Pl. pyroxenite	30	35	25	10	0	0.355	62	2.37	3.87	2.73
M11-6	Sp. pyroxenite	30	10	55	5	0	0.379	86	1.71	1.96	1.74
M11-8	Sp. pyroxenite	40	25	30	5	0	0.402	55	2.2	2.27	2.00
M11-12C	Pl. pyroxenite	35	30	15	15	5	0.208	84	1.68	2.55	1.81
M11-7	Sp. pyroxenite	40	20	35	5	0	0.298	64	1.72	2.35	1.65
M11-12A	Pl. pyroxenite	45	20	15	15	5	0.182	105	1.56	2.74	1.85

Field-based lithotypes: *Sp. pyroxenite* spinel pyroxenite, *Pl. Pyroxenite* plagioclase pyroxenite, *Ol* olivine, *Cpx* clinopyroxene, Opx, orthopyroxene, *Plagio* plagioclase, *Sp* spinel, *N*° grain cumber, *PfJ* fabric strength of single crystallographic pole

We performed structural electron backscatter diffraction (EBSD) mapping of all pyroxenite samples at Géosciences Montpellier (University of Montpellier, France). Mineral major element analyses (EPMA) have been performed at the Dipartimento di Scienze della Terra, University of Milano (Italy) and mineral trace element analyses (LA–ICP–MS) have been performed at C.N.R., Istituto di Geoscienze e Georisorse, Unità di Pavia (Italy). Detailed methodologies for EBSD, major and trace elements analyses can be found in Supplementary Material.

In the pyroxenites, clinopyroxenes and orthopyroxenes often show exsolutions of the conjugate pyroxene (see "Petrography of the pyroxenite layers"). Major element in situ EPMA analyses were performed on mineral cores, rims and pyroxene exsolutions and are further referred to as "spot analyses". To reconstruct the major element composition of primary pyroxene porphyroclasts, prior to the sub-solidus exsolution stage, we performed areal quantitative analyses of exsolved clinopyroxene and orthopyroxene porphyroclastic cores, from 100 × 100 µm to 300x300 µm (Fig. S1). The areal analyses that respect the stoichiometry of the bulk mineral (clinopyroxene or orthopyroxene) are used as a reference for the primary composition of the pyroxene core. These analyses have been performed at the Dipartimento di Scienze della Terra, dell'Ambiente e della Vita (DISTAV), University of Genoa using a TESCAN VEGA3 Scanning Electron Microscope equipped with an Energy Dispersive X-ray analyser (accelerating power 20 kV).

Petrography of the pyroxenite layers

The pyroxenite layers are mainly websterites (Table 1). The primary mineral assemblage consists of coarse-grained clinopyroxene, orthopyroxene and spinel (Figs. 1, 2). Clinopyroxenes are coarse porphyroclasts, partially corroded by interstitial olivine (Fig. 2a). They are deformed, as evidenced by undulatory extinction, and display exsolutions of variable sizes, from thin lamellas of orthopyroxene (Figs. 2e, S1) to 100 µm-size orthopyroxene + plagioclase aggregates (Fig. 2f). Orthopyroxenes are found in two different microstructural situations: (1) coarse porphyroclasts partially corroded by interstitial olivine (opx1, Fig. 2b), showing undulatory extinctions and thin lamellas of clinopyroxene exsolutions (Fig. S1), and (2) interstitial to poikilitic orthopyroxene, associated with interstitial plagioclase, often forming orthopyroxene + plagioclase intergrowths (opx2, Fig. 2c, d). Interstitial orthopyroxene is mainly observed in the plagioclase pyroxenite samples showing extensive impregnation features (M11-5B, M11-12A, M11-12C). These interstitial orthopyroxenes are mostly undeformed and show few to no exsolutions of clinopyroxene. Olivines are always interstitial, showing lobate contacts against clinopyroxene and orthopyroxene porphyroclasts (Fig. 2a, b). They are deformed and often display kink bands. Plagioclases are always undeformed and occur as interstitial to poikilitic crystals showing lobate contacts against both pyroxene porphyroclasts and interstitial olivine (Fig. 2d). In the pyroxenite layers, they are mostly replaced by low-grade alteration products (Fig. 2c, d). Spinels are mostly black to brownish granular millimetre-size crystals associated with porphyroclastic pyroxenes and partially dissolved by interstitial olivine and plagioclase.

The main petrological features characterizing the pyroxenite layers therefore indicate that: (1) spinel-facies reactive porous flow led to the partial dissolution of the porphyroclastic pyroxenes and to the interstitial crystallization of olivine; (2) plagioclase-facies impregnation led to enrichments in interstitial plagioclase and orthopyroxene at the expense of the porphyroclastic pyroxenes and interstitial olivine; (3) the pyroxenites were partially reequilibrated to plagioclase-facies sub-solidus conditions.

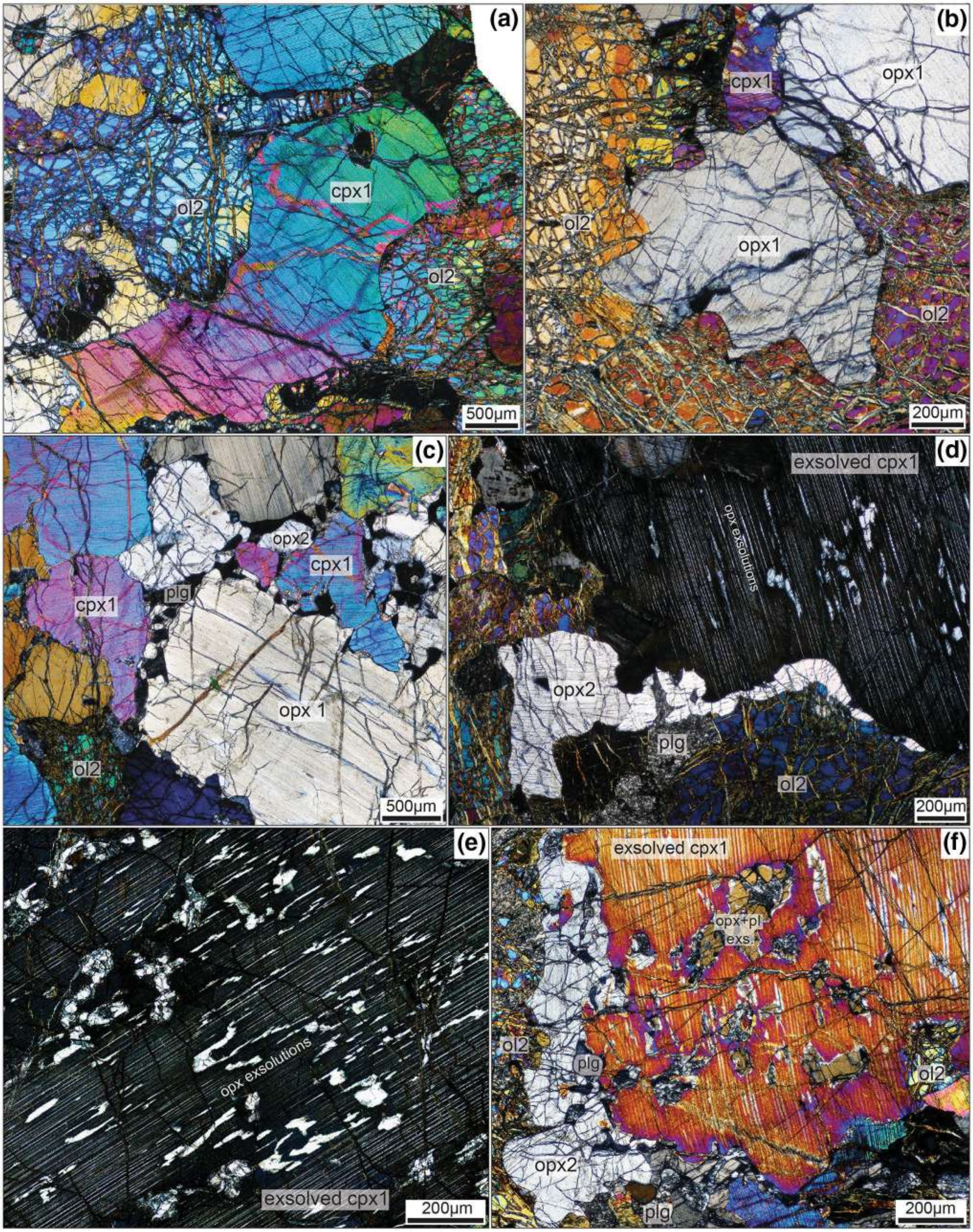
(a)
cpx1
ol2
ol2
500μm
(b)
cpx1
opx1
ol2
opx1
ol2
200μm
(c)
opx2
cpx1
plg
cpx1
opx 1
ol2
500μm
(d)
exsolved cpx1
opx exsolutions
opx2
plg
ol2
200μm
(e)
opx exsolutions
exsolved cpx1
200μm
(f)
exsolved cpx1
opx+pl exs.
ol2
plg
ol2
opx2
plg
200μm

◂**Fig. 2** Representative microstructures of the spinel and plagioclase pyroxenites. **a** Spinel pyroxenite. Interstitial olivine develops embayments on porphyroclastic clinopyroxene; **b** spinel pyroxenite. Interstitial olivine develops embayments on porphyroclastic orthopyroxene; **c** plagioclase pyroxenite. Interstitial plagioclase + orthopyroxene intergrowths develops embayments on interstitial olivine and porphyroclastic clinopyroxene; **d** plagioclase pyroxenite. Interstitial plagioclase and orthopyroxene develop embayments on interstitial olivine and exsolved porphyroclastic clinopyroxene; **e** plagioclase pyroxenite. Extensive orthopyroxene exsolution development in porphyroclastic clinopyroxene; **f** plagioclase pyroxenite. Interstitial orthopyroxene and plagioclase intergrowth at the expense of a porphyroclastic clinopyroxene showing extensive [orthopyroxene + plagioclase] exsolutions

Crystallographic preferred orientation of olivine

Pyroxenite layers all show a clear olivine Crystallographic Preferred Orientation (CPO) pattern. Despite the large grain size, the well-defined patterns allow to investigate qualitatively the olivine CPO (grain number ranging from 42 to 105 crystals; Table 1). Figure 3 shows the modal composition, olivine CPO, grain number and BA-index (representative of the qualitative CPO symmetry of the olivine [100] and [010] axes; Mainprice et al. 2014) of all the pyroxenite layer samples.

Olivines in the pyroxenite layers are characterized by an axial-[010] CPO (BA-index < 0.45; Mainprice et al. 2014; Tommasi and Ishikawa 2014), with [010] being the strongest axis orientation, normal to the pyroxenite layer plane (Fig. 3). Such axial-[010] olivine CPOs have been previously described in impregnated peridotites (Ben Ismail et al. 2001; Le Roux et al. 2008; Tommasi et al. 2008), replacive olivine-rich gabbroic rocks (Higgie and Tommasi 2012, 2014) and experiments of melt segregation during deformation (Holtzman et al. 2003). Recently, Basch et al. (2018) performed a microstructural study of the Mt. Maggiore ultramafic body and interpreted the olivine axial-[010] CPO in reacted spinel peridotite (olivine-enriched harzburgite), spinel dunite, olivine-rich troctolite, and troctolite as an indicator of deformation in the presence of melt (Holtzman et al. 2003; Le Roux et al. 2008; Kaczmarek and Tommasi 2011).

Major and trace element mineral compositions

Major and trace element compositions of clinopyroxene, orthopyroxene, spinel, olivine and plagioclase from the studied pyroxenite layers are reported in Table S1–5 of Supplementary Material.

Clinopyroxene Porphyroclast spot analyses (Table S1) are characterized by relatively high Al_2O_3 concentrations, progressively decreasing at increasing Mg-value from cores (Mg# = 88.0–90.5 mol%; Al_2O_3 = 4.57–7.24 wt%), to rims (Mg# = 89.3–91.4 mol%; Al_2O_3 = 3.20–5.95 wt%), to clinopyroxene exsolutions within orthopyroxene (Fig. 4a; Mg# = 90.3–92.0 mol%; Al_2O_3 = 2.24–4.88 wt%). All spot analyses of clinopyroxene show low Na_2O and TiO_2 (Fig. 4b; Na_2O = 0.08–0.24 wt%; TiO_2 = 0.2–0.4 wt%), and high CaO and Cr_2O_3 contents (CaO = 20.12–24.30 wt%; Cr_2O_3 = 0.7–1.3 wt%). Clinopyroxene areal analyses of exsolved cores show compositions similar to spot core analyses in terms of Mg-value (Mg# = 89–89.6 mol%; Fig. 4a, b), Al_2O_3 (5.96–7.07 wt%; Fig. 4a) and Na_2O concentrations (0.08–0.16 wt%; Fig. 4b), but they show higher MgO (19.53–19.81 wt%) and FeO (4.26–4.36 wt%), and lower CaO (18.10–18.44 wt%) concentrations, consistent with the bulk clinopyroxene composition prior to orthopyroxene exsolution. Porphyroclastic cores (both areal and spot analyses; Fig. 4a, b) show similar Mg-values, Al_2O_3 compositions and lower Na_2O contents relative to clinopyroxenes analysed in spinel peridotites from Mt. Maggiore (Basch et al. 2018) and in spinel websterites from the South-West Indian Ridge (Dantas et al. 2007). Clinopyroxenes analysed in variably reequilibrated plagioclase websterites from the Lena Trough (Fig. 4a, b) show a range of variation of Al_2O_3 and Mg-value similar to the core-rim variation in the Mt. Maggiore pyroxenites but higher Na_2O concentrations (Laukert et al. 2014). Trace element compositions of clinopyroxene porphyroclastic cores (Fig. 5a) show strong LREE depletion (Ce_N/Sm_N = 0.015–0.037) and flat MREE-HREE patterns (Yb_N = 8.4–10.4 times C1), similar to clinopyroxenes analysed in plagioclase peridotites and gabbronoritic veinlets from Mt. Maggiore (Rampone et al. 2008; Basch et al. 2018), plagioclase websterites from the Lena Trough (Laukert et al. 2014), and spinel websterites from the South-West Indian Ridge (Dantas et al. 2007). These LREE-depleted compositions do not correspond to a MORB-type composition (Fig. 5a), unlike clinopyroxenes reported in websterites from the Internal Ligurian ophiolites (Sanfilippo and Tribuzio 2011) and in part of the websterites from the South-West Indian Ridge (Warren et al. 2009).

Orthopyroxene Porphyroclast spot analyses (Table S2) show high Mg-value, Al_2O_3, and Cr_2O_3 contents in orthopyroxene cores (Fig. 4c, d; Mg# = 88.8–90.1 mol%; Al_2O_3 = 2.22–4.90 wt%; Cr_2O_3 = 0.47–0.95 wt%) and rims (Mg# = 88.7–90.1 mol%; Al_2O_3 = 1.79–4.85 wt%; Cr_2O_3 = 0.43–0.93 wt%). Orthopyroxene exsolutions in clinopyroxene show similar Mg-values, Cr_2O_3 compositions (Mg# = 88.4–89.9 mol%; Cr_2O_3 = 0.55–0.87 wt%; Fig. 4c, d), and lower Al_2O_3 contents (Al_2O_3 = 1.71–3.76 wt%; Fig. 4c, d) relative to the orthopyroxene porphyroclastic cores and rims. Orthopyroxene porphyroclastic cores and rims show variable CaO concentrations (CaO = 0.6–1.4 wt%), as a function of the extent of clinopyroxene exsolution. Orthopyroxene areal analyses of exsolved porphyroclastic cores show

Fig. 3 Olivine Crystallographic Preferred Orientation of plagioclase pyroxenites from the Mt. Maggiore peridotitic body. One point-per-grain equal-area, lower hemisphere stereographic projections. The colour bar is scaled to the maximum concentration of the three crystallographic axes. BA refers to the calculated BA-index (Mainprice et al. 2014), *n* to the grain number

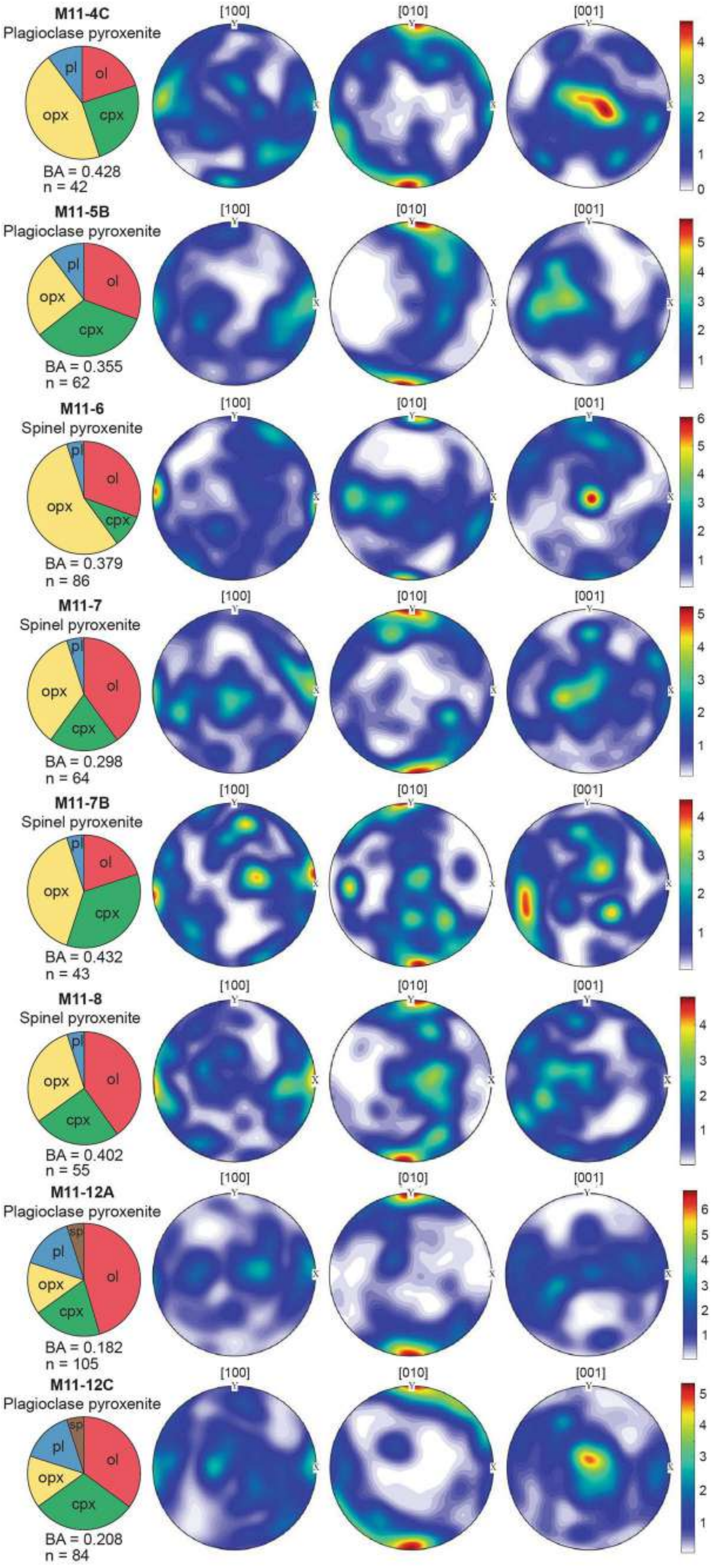

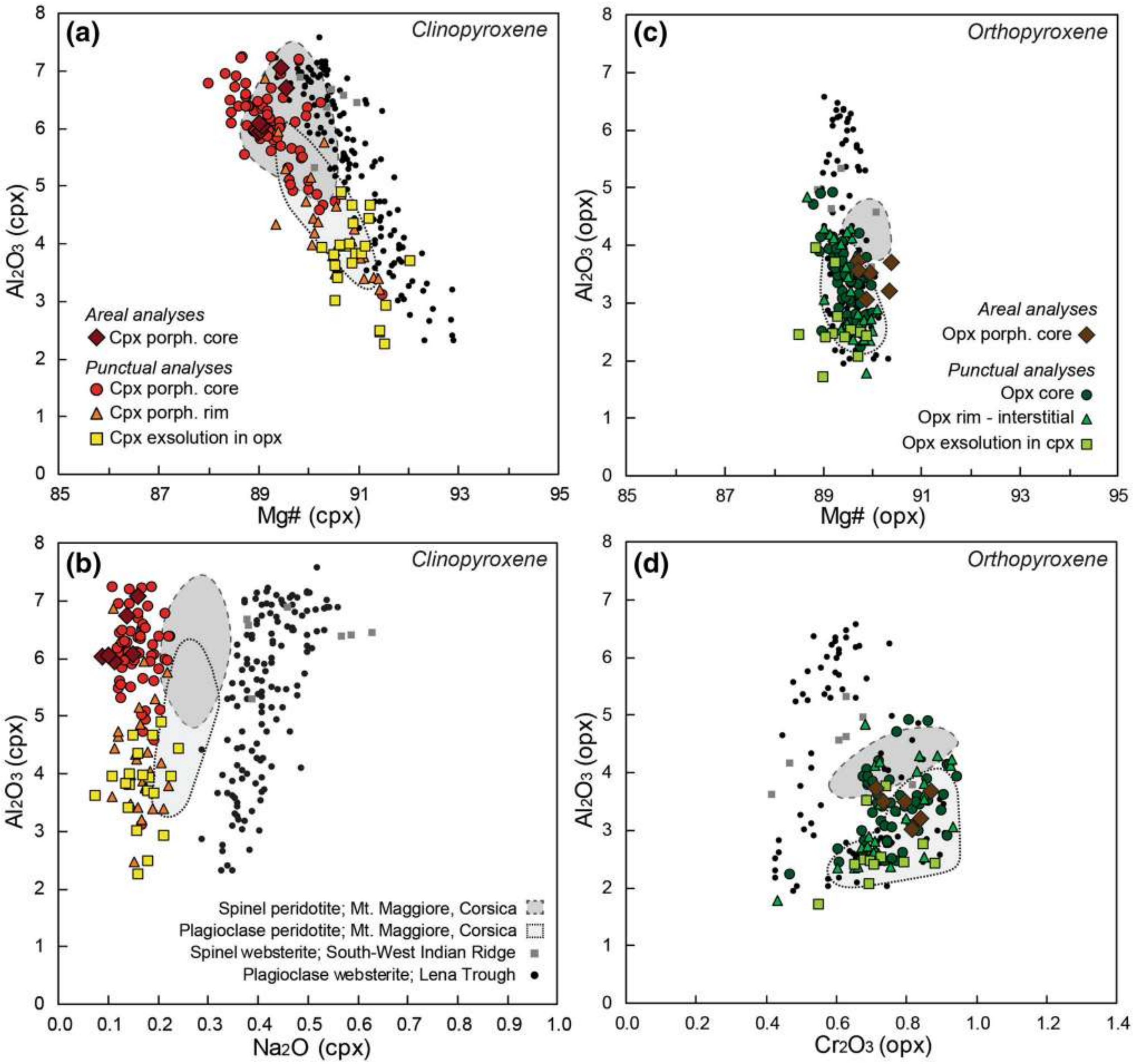

Fig. 4 Major element concentrations of clinopyroxene (**a**, **b**) and orthopyroxene (**c**, **d**) in spinel pyroxenites and plagioclase pyroxenites. **a** Mg# (mol%) vs Al_2O_3 (wt%); **b** Na_2O vs Al_2O_3 (wt%); **c** Mg# (mol%) vs Al_2O_3 (wt%); **d** Cr_2O_3 vs Al_2O_3 (wt%). Compositional fields of Mt. Maggiore spinel and plagioclase peridotites after Basch et al. (2018), and single analyses of spinel websterites from South-West Indian Ridge (Dantas et al. 2007) and plagioclase websterites from Lena Trough (Laukert et al. 2014)

higher CaO (CaO = 2.1–2.5 wt%) and lower SiO_2 contents (SiO2 = 53.9–54.3 wt%) than the spot porphyroclastic core analyses. Interstitial and poikilitic orthopyroxenes also show higher CaO contents in crystal cores (CaO = 1.0–2.5 wt%) and rims (CaO = 0.9–1.5 wt%) than the orthopyroxene porphyroclasts. The analysed orthopyroxene porphyroclastic core compositions are similar to the ones reported in plagioclase websterites from the Lena Trough (Fig. 4c, d; Laukert et al. 2014) and to orthopyroxenes analysed in the associated plagioclase peridotites from Mt. Maggiore (Fig. 4c, d; Basch et al. 2018). Porphyroclastic and interstitial orthopyroxene cores (Fig. 5b) all show rather strong LREE depletion ($Ce_N/Yb_N = 0.001–0.003$), and MREE-HREE concentrations ($Yb_N = 2.3–3.1$ times C1) similar to orthopyroxenes analysed in spinel websterites from South-West Indian Ridge (Dantas et al. 2007), in plagioclase websterites from Lena Trough (Laukert et al. 2014) and in plagioclase peridotites from Mt. Maggiore (Basch et al. 2018).

Plagioclase cores (Table S3) are characterized by anorthite-rich compositions (An = 93.1–95.4 mol%), consistent

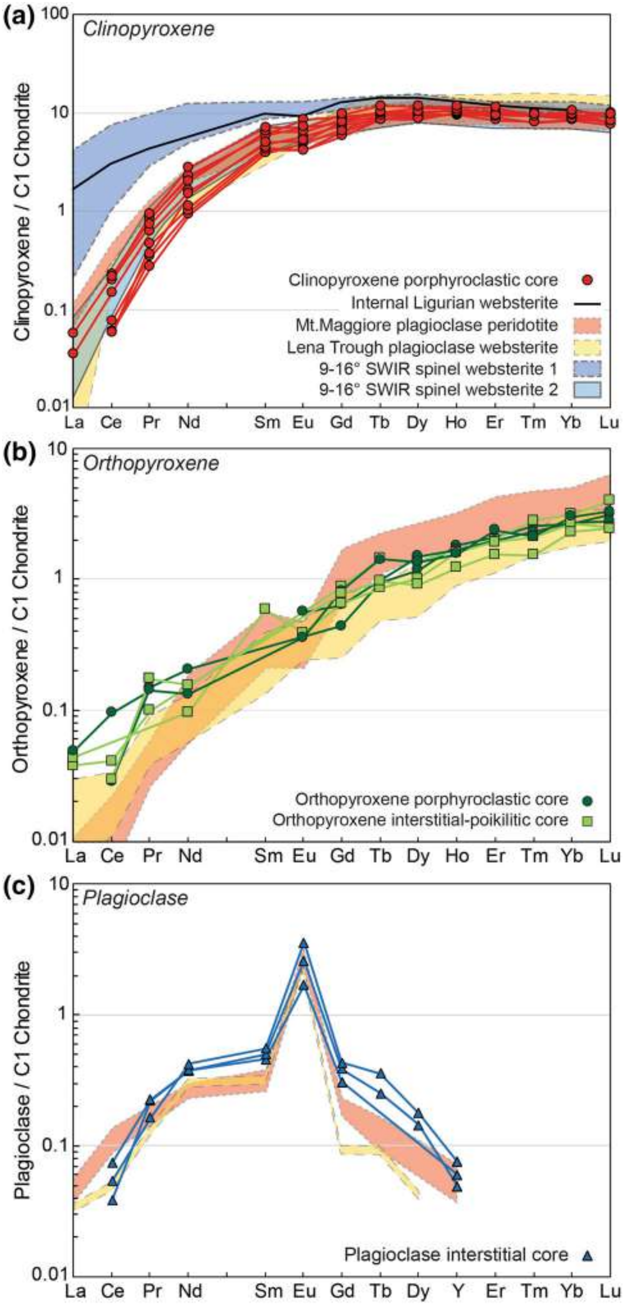

Fig. 5 C1-normalized REE composition of rock-forming minerals in the impregnated pyroxenites. **a** Porphyroclastic clinopyroxene core, **b** porphyroclastic and interstitial orthopyroxene core; **c** interstitial plagioclase core. C1-chondrite normalization values after Sun and McDonough (1989). Internal Ligurian websterite after Sanfilippo and Tribuzio (2011), compositional field for Mt. Maggiore plagioclase peridotites after Basch et al. (2018), plagioclase websterite from Lena Trough after Laukert et al. (2014), and spinel websterite 1 and 2 from 9°–16° South-West Indian Ridge after Warren et al. (2009) and Dantas et al. (2007), respectively

with their low Na_2O concentrations ($Na_2O = 0.52–0.78$ wt%). The Na_2O contents decrease towards the rims of the crystals, leading to more anorthitic rim compositions ($Na_2O = 0.32–0.52$ wt%; An = 95.4–97.1 mol%). Plagioclase cores (Fig. 5c) all show strong LREE and HREE depletion ($Ce_N/Sm_N = 0.08–0.15$; $Sm_N = 0.45–0.55$ times C1; $Y_N = 0.08–0.12$ times C1) similar to plagioclase compositions reported in plagioclase websterites from the Lena Trough (Laukert et al. 2014) and in the associated plagioclase peridotites from Mt. Maggiore (Basch et al. 2018).

Olivine (Table S4) shows a narrow compositional range in all pyroxenite layers, at high Forsterite contents (Fo = 88.9–90.2 mol%), similar to the olivine compositions reported in the associated spinel peridotites, plagioclase peridotites, spinel dunites and troctolites from Mt. Maggiore (Fo = 89.5–90.2 mol%; Basch et al. 2018).

Spinel (Table S5) shows variable compositions between spinel pyroxenite and plagioclase pyroxenite. In the spinel pyroxenites, spinels show Cr-values, Mg-values and TiO_2 contents (Cr# = 15 mol%; Mg# = 72 mol%; $TiO_2 = 0.12$ wt%) similar to what was documented in spinel websterites from the South-West Indian Ridge (Dantas et al. 2007). In the plagioclase pyroxenites, spinels show higher Cr-values and TiO_2 contents (Cr# = 32–42mol%; TiO2 = 0.32–0.40 wt%) and lower Mg-values (Mg# = 62–67 mol%).

Geothermobarometric estimates

Equilibration temperatures of the different stages recorded in the pyroxenite layers were obtained using two-pyroxene Fe–Mg geothermometers (Brey and Köhler 1990; Taylor 1998) and Ca-in-orthopyroxene geothermometer (Brey and Köhler 1990). The calculated equilibrium temperature estimates are representative of: (1) the formation of the pyroxenite layers, using areal analyses of orthopyroxene and clinopyroxene as representative of their primary composition (Fig. S1); (2) the plagioclase-facies impregnation stage of the pyroxenite, using spot analyses of interstitial orthopyroxene cores (using Ca-in-opx geothermometer). These estimates are complemented by coupled orthopyroxene-clinopyroxene cores from the gabbronorite segregations found within the plagioclase peridotites (data after Rampone et al. 2008; Basch et al. 2018); (3) the plagioclase-facies sub-solidus reequilibration, using spot analyses of variably exsolved cores and rims of porphyroclastic clinopyroxene and orthopyroxene, and coupling clinopyroxene and orthopyroxene exsolutions (Fig. 2e, f).

Additionally, we obtained geobarometric estimates of the plagioclase-bearing equilibrium applying the FACE geobarometer to clinopyroxene-orthopyroxene-plagioclase-olivine association (Fumagalli et al. 2017). We emphasize, however, that the FACE geobarometer was calibrated using experimental data on plagioclase peridotite compositions (Borghini et al. 2010, 2011; Fumagalli et al. 2017), meaning that our equilibration pressure calculations for olivine-bearing gabbronoritic compositions represent indicative pressure estimates. This mineralogical association is found in different microstructural occurrences giving pressure estimates of: (1) plagioclase-facies impregnation stage of the pyroxenite represented by the gabbronoritic segregation mineral cores (data after Rampone et al. 2008; Basch et al. 2018); (2) plagioclase-facies sub-solidus reequilibration represented by the mineral reequilibrated rims in impregnated pyroxenites. We used porphyroclastic rims of clinopyroxene, rims of interstitial olivine, and rims of interstitial orthopyroxene and plagioclase; (3) advanced stages of sub-solidus reequilibration represented by large orthopyroxene + plagioclase exsolution aggregates (Fig. 2f). The clinopyroxene and olivine considered in the calculation are the reequilibrated clinopyroxene at the contact with the exsolution and the rims of interstitial olivine.

The geothermobarometric estimates obtained are summarized in Table 2. The areal analyses of porphyroclastic clinopyroxene and orthopyroxene, representative of the spinel-facies formation of the pyroxenites, yield the highest equilibrium temperatures of 1210–1300 °C. The plagioclase-facies melt impregnation process is characterized by high equilibrium temperatures of 1080–1290 °C, at pressures of 6.4–6.6 kbar. The high variability of the temperature estimates is the expression of different extents of exsolution of the interstitial orthopyroxene cores (lower temperatures represent higher extents of exsolution). The sub-solidus reequilibration calculated at the rims of the porphyroclastic and interstitial crystals yield lower equilibrium temperatures and pressures of 880–1080 °C at 4.2–4.6 kbar. The more extensive sub-solidus reequilibration represented by the plagioclase + orthopyroxene exsolution is characterized by low equilibrium temperatures of 780–900 °C at 2.9–3.1 kbar.

Table 2 Geothermobarometric estimates of different processes recorded in the pyroxenite layers

	Temperature (°C)		Pressure (kbar)
	opx-cpx[a]	opx[b]	cpx-opx-pl-ol[c]
Formation of pyroxenites	1210–1240	1260–1300	–
Melt impregnation	–	1080–1290	6.4–6.6
Sub-solidus reequilibration	880–1050	900–1080	4.2–4.6
Extensive sub-solidus reequ.	780–900	900–980	2.9–3.1

See the text for more detail

[a] After Brey and Köhler (1990) and Taylor (1998)

[b] After Taylor (1998)

[c] After Fumagalli et al. (2017)

Discussion

What do the pyroxenite layers represent?

Previous studies of the Mt. Maggiore peridotitic massif described a complex melt–rock interaction history recorded in the spinel and plagioclase peridotites, dunites and troctolites (Rampone et al. 1997, 2008; Müntener and Piccardo 2003; Piccardo and Guarnieri 2010; Basch et al. 2018). The evidence that pyroxenite layers record the processes of melt–rock interaction documented in the associated peridotites (e.g., Basch et al. 2018), indicates that their formation predates the spinel- to plagioclase-facies melt–rock interaction history.

In the studied pyroxenites, olivine is always interstitial and shows lobate contacts against clinopyroxene and orthopyroxene porphyroclasts (Fig. 2a, b). These microstructures are progressively more developed the more the pyroxenite layer is dissolved (Fig. 1c, d). Thus, based on petrographic evidence and supported by previous microstructural studies of the reactive percolation process within the host peridotites (e.g., Basch et al., 2018), we infer that olivine is entirely the product of the spinel-facies reactive porous flow. The relationship between interstitial olivine and the reactive porous flow process is also suggested by the axial-[010] olivine CPO measured in the pyroxenite layers ($0.18 < \text{BA-index} < 0.43$; Fig. 3). Similar axial-[010] olivine CPO were reported in the most reacted spinel harzburgites and spinel dunites from Mt. Maggiore ($\text{BA-index} < 0.5$; Basch et al. 2018) and interpreted as a melt-assisted deformation feature associated with the spinel-facies reactive porous flow process. Although such an olivine CPO (Fig. 3) within the pyroxenite layers does not require the crystallization of olivine from the melt, but rather its presence during melt-assisted deformation, we infer that together with the petrographic evidence, it supports crystallization of the olivine during reactive porous flow.

Within the pyroxenite layers, melt impregnation led to the interstitial crystallization of plagioclase and orthopyroxene at the expense of olivine and clinopyroxene porphyroclasts (Fig. 2c, d). These microstructural observations imply that plagioclase (10–15 vol%; Table 1) and at least part of the orthopyroxene abundance measured in the pyroxenites (15–50 vol%; Table 1) are the products of melt impregnation at plagioclase-facies conditions. Based on microstructural and EBSD map observations, we thus infer that the pyroxenite layers were primarily formed by large porphyroclastic clinopyroxene (~ 60 to 90 vol%), porphyroclastic orthopyroxene (~ 10 to 30 vol%) and spinel (~ 0 to 10 vol%).

Pyroxene porphyroclast cores in the studied pyroxenites have Al_2O_3 compositions (Fig. 4) similar to those of South-West Indian Ridge and Lena Trough websterites (Seyler et al. 2001; Dantas et al. 2007; Laukert et al. 2014). These oceanic pyroxenites associated with residual peridotites were interpreted as formed by relatively high-pressure melt segregations (> 7 kbar; Dantas et al. 2007; Laukert et al. 2014). Experimental studies of MORB crystallization evidenced the possible formation of websterites during fractional and equilibrium crystallization processes occurring at pressures of 7–10 kbar (e.g. Villiger et al. 2004, 2007; Husen et al. 2016). The crystallization of websterites (clinopyroxene-orthopyroxene-spinel) is related to early saturation of pyroxenes, as a result of the increasing stability of pyroxenes and decreasing stability of plagioclase at increasing pressure. Villiger et al. (2004) also documented an increase in Al_2O_3 concentration in clinopyroxene and orthopyroxene with pressure (up to 7 wt% Al_2O_3 in clinopyroxene at 10 kbar). We infer that the primary modal composition, and the high Al_2O_3 contents and Mg-values in porphyroclastic pyroxenes forming the Mt. Maggiore pyroxenites resulted from high-pressure fractionation (8–10 kbar) of a migrating melt.

The pyroxene porphyroclasts show Na_2O-poor (Fig. 4b) and LREE-depleted compositions (Fig. 5a, b), indicative of depleted parental melts (Fig. 6). In terms of LREE depletion, computed melts in equilibrium with clinopyroxenes are consistent with single-melt increments formed after 5–7% fractional melting of a Depleted Mantle source (Fig. 6; Workman and Hart 2005; Warren 2016), as proposed for the melts percolating in the host peridotites (Rampone et al. 2008; Basch et al. 2018). A similar origin from depleted single-melt increments was inferred for spinel websterites from the Southwest Indian Ridge (Dantas et al. 2007). The MREE-HREE enrichment observed in the clinopyroxene porphyroclasts (Fig. 6), relative to the clinopyroxene in equilibrium with single-melt increments, can be ascribed to the sub-solidus exsolution process in clinopyroxenes. Hellebrand et al. (2005) documented strong enrichments in clinopyroxene trace elements during extensive clinopyroxene exsolution, as what is observed at Mt. Maggiore (Fig. 2d–f). Moreover, Rampone et al. (2008) and Basch et al. (2018) modeled the REE evolution of melts percolating during an olivine-dissolving assimilation-fractional crystallization process and documented increasing MREE-HREE concentrations at constant LREE depletion. A reequilibration between the pyroxene porphyroclasts and the melt modified during reactive porous flow could therefore participate in the HREE enrichments observed in the pyroxenites.

Interstitial plagioclase and orthopyroxene show Na_2O-poor and LREE-depleted compositions (Fig. 5b, c), similar to the porphyroclastic pyroxenes forming the primary mineral assemblage. This suggests a depleted composition of the impregnating melt, as previously documented in the host impregnated plagioclase peridotites (Rampone et al. 1997, 2008, 2019; Basch et al. 2018).

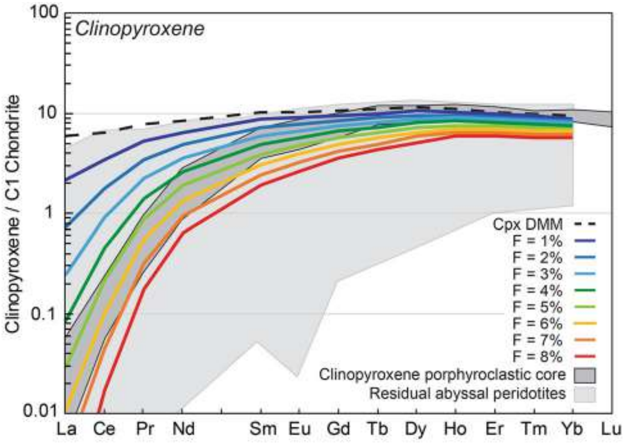

Fig. 6 C1-normalized REE spectra of residual clinopyroxenes after variable degrees (F) of fractional melting. Clinopyroxene DMM compositions are from Warren (2016) and partition coefficients from Basch et al. (2018). C1-chondrite normalization values after Sun and McDonough (1989). Also reported is the compositional field defined by clinopyroxenes porphyroclastic cores in the spinel websterites and the compositional field of residual abyssal peridotites after Warren (2016)

In summary, both the parental melts of pyroxenites and the melts involved in the subsequent percolation were characterized by Na_2O-poor, LREE-depleted compositions, consistent with unaggregated melt increments rather than aggregated MORBs (Figs. 4, 5). This implies that they represent the continuous evolution of similar melts leading to different processes (pyroxenite segregation and later melt–rock interaction) during their upward migration at changing pressure–temperature conditions from spinel-facies to plagioclase-facies depths. Such a continuity implies not only a temporal but also a spatial evolution of the type of process occurring during percolation of the melts in a mantle column in exhumation. To support the genetic relation and the continuity between the formation of pyroxenites and the subsequent melt–rock interaction history, we modeled all the documented processes in sequence, i.e.: (1) formation of single-melt increments after 6% mantle decompressional fractional melting; (2) high-pressure segregation of pyroxenites; (3) spinel-facies reactive porous flow, (4) plagioclase-facies melt impregnation. We used the pMELTS thermodynamic program (Ghiorso et al. 2002) that allows to assess the evolution of the melt phase saturation and chemical composition, and the major element composition of the fractionated phases.

Basch et al. (2018) recently modeled the REE compositional evolution of depleted melts during the melt–rock interaction history documented at Mt. Maggiore. However, major element modeling of the formation of melt during decompressional melting and subsequent chemical evolution during percolation was never performed in oceanic environments. The Mt. Maggiore peridotitic massif provides a good field (Fig. 1) and microstructural control (Fig. 2) on the chronology of the different processes documented within the pyroxenites, thus allowing to test the described dynamic model.

Formation of the depleted single-melt increments

To simulate decompressional mantle melting and major element composition of single-melt increments during fractional melting, we performed a model of adiabatic decompression of a Depleted MORB Mantle (DMM; Workman and Hart 2005). An adiabatic temperature gradient (~ 0.8 °C/km; e.g. Hebert and Montési 2010) is imposed to the DMM mantle, upwelling from 25 kbar, 1400 °C to 9 kbar, 1360 °C. The adiabat crosses the DMM solidus at 13.6 kbar, 1372 °C, therefore initiating the mantle melting process (Fig. S3). At 10 kbar, 1362 °C, fractional melting reaches 6% (Fig. S3), which is consistent with the mineral compositions documented in the residual peridotites (e.g. Rampone et al. 2008) and to the parental melt involved in the formation of pyroxenites and melt–rock interaction history (e.g. Basch et al. 2018). At this depth (~ 30 km) we infer that the residual mantle was incorporated in the TBL and started cooling conductively, which in turn led to the cessation of the melting process (e.g. Langmuir et al. 1992; Shen and Forsyth 1995; Niu 1997; Niu and Hékinian 1997; Langmuir and Forsyth 2007; Montési and Behn 2007; D'Errico et al. 2016). The narrow range of pressure involving mantle melting (13.6–10 kbar) and the thick TBL inferred are consistent with the cold ultra-slow-spreading environment described at Mt. Maggiore (e.g. Rampone et al. 2014, 2019).

In Fig. 7, we compare the chemical evolution of single-melt increments and aggregated melts along progressive melting. At increasing degree of melting, the melt compositions show decreasing concentrations of Al_2O_3, Na_2O and increasing SiO_2, CaO and Ca# (Ca# = Ca/(Ca + Na) mol%). Single-melt increments show larger compositional variations than the aggregated melts, which are calculated as weighted mass balance of the different single-melt increments (Fig. 7; Table S6). Both single-melt increments and aggregated melts show high Mg# (~ 75 to 76 mol%), consistent with primitive MORB compositions and/or unaggregated melts formed by multi-stage melting processes, as previously reported in experimental mantle melting studies (Duncan and Green 1987; Falloon and Green 1988; Kinzler and Grove 1992; Hirose and Kushiro 1993) and in natural samples and melt inclusions (Duncan and Green 1980; Sobolev and Shimizu 1993). The strongest compositional differences are observed for Na_2O, CaO and therefore Ca#, that is much higher in the single-melt increments, in comparison with the aggregated melts (+ 15 mol% after 6% total melting). The composition of the selected melt, i.e. single-melt increment after 6% of DMM melting (light red stripe in Fig. 7) is given in Table 3 and shows high Mg-value (Mg# = 75 mol%), CaO-rich (CaO = 13 wt%), Na_2O-poor compositions (Na_2O = 0.7 wt%), consistently with the melt compositions documented at Mt. Maggiore (Basch et al. 2018).

High-pressure segregation of the pyroxenite layers

To constrain the magmatic formation of the pyroxenite layers, we performed a model of high-pressure reactive fractional crystallization. We used as starting melt composition the single-melt increment calculated in the previous modeling stage after 6% DMM melting (Table 3). This melt fraction forms at 1362 °C, 10 kbar while the mantle likely enters the TBL. We model the reactive fractional crystallization of this melt during its percolation in the lithospheric mantle from 10 to 9.5 kbar, at temperatures decreasing from 1360 to 1310 °C. The temperatures assumed for the model are slightly higher than the geothermometric estimates obtained for porphyroclastic pyroxene pairs (up to 1300 °C; Table 2). We infer that the difference between the modeled and calculated temperatures is the result of analytical uncertainty in the measurement of areal analyses and in the geothermometric estimates. The selected melt is only saturated in clinopyroxene at the pressures considered in our model. This model assumes the assimilation of 0.2 g/ °C of host lherzolite (ol:opx:cpx:spinel = 58:27:12:3; computed by pMELTS from the most fertile host lherzolite bulk composition, after Piccardo and Guarnieri 2010). Small amounts of mantle assimilation are necessary in our model to reach orthopyroxene saturation in the melt. We infer that the reactivity of this melt towards the host lherzolite is the result of the decompression and cooling of these newly formed melts. Such a model of reactive melt percolation assuming the assimilation of a bulk peridotite have been previously proposed by Dijkstra et al. (2003), Collier and Kelemen (2010) and Sanfilippo et al. (2016) to simulate deep melt percolation within the mantle.

Figure 8 shows the modal composition of the crystallized and assimilated mineral phases in the reactive fractional crystallization model. After 20% fractionation at 1335 °C (Fig. 8a), the melt crystallizes a spinel websterite formed by clinopyroxene (~ 80 vol%), orthopyroxene (~ 15 vol%), spinel (~ 3 vol%), and minor olivine (~ 2 vol%) (Fig. 8b). The computed modal compositions reproduce well the inferred modal compositions of the primary pyroxenite layers at Mt. Maggiore. The ratio mass assimilated/mass crystallized remains low and rather constant during the whole process of reactive fractional crystallization (Ma/Mc ~ 0.2; Fig. 8b), and thus indicates that the process is dominated by melt fractionation, at decreasing melt mass.

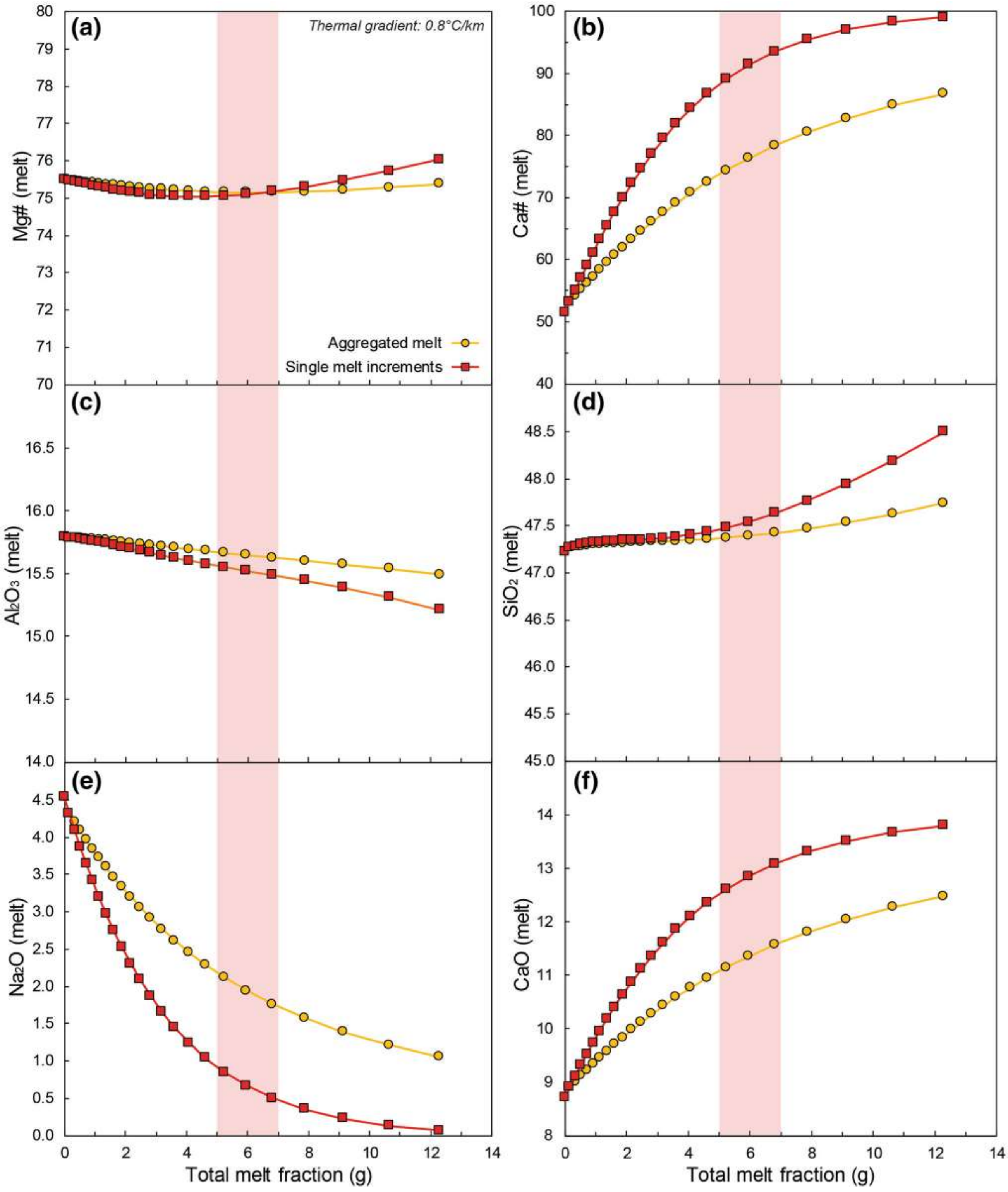

Fig. 7 Total melt fraction (g) vs composition of the single-melt increments and aggregated melts formed during the pMELTS modeling of DMM mantle (Workman and Hart 2005) adiabatic decompression. **a** Mg# (mol%); **b** Ca# (mol%); **c** Al_2O_3 (wt%); **d** SiO_2 (wt%); **e** Na_2O (wt%); **f** CaO (wt%). Considered thermal gradient of 0.8 °C/km

Table 3 Initial melt compositions used in the pMELTS thermodynamic models of reactive percolation

Melt composition	*T* (°C)	*P* (kbar)	SiO_2	TiO_2	Al_2O_3	Fe_2O_3	Cr_2O_3	FeO	MnO	MgO	NiO	CaO	Na_2O	Total	Mg#	Ca#
Pyrox. Formation	1362.5	10	47.54	0.81	15.52	0.84	0.05	8.06	0.01	13.64	0.01	12.86	0.67	100.0	75.10	91.40
Reac. porous flow	1335	9.75	46.73	0.91	17.04	1.33	0.00	8.46	0.02	12.55	0.02	12.14	0.80	100.0	72.57	89.37
Melt impregnation	1290	7.00	47.48	0.92	17.39	1.35	0.00	8.21	0.00	11.38	0.00	12.45	0.81	100.0	71.19	89.51

Mg# = Mg/(Mg + Fe); Ca# = Ca/(Ca + Na)

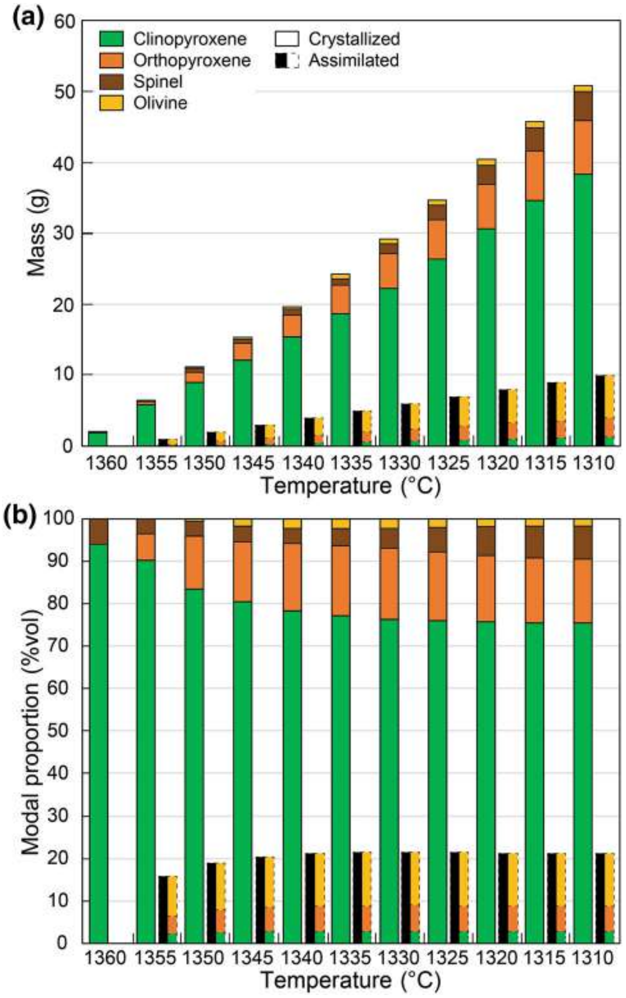

Fig. 8 Temperature (°C) vs cumulated modal composition of the assimilated and fractionated phases during the pMELTS model of reactive fractional crystallization from 10 kbar, 1360 °C to 9 kbar, 1310 °C. Initial melt composition is the single-melt increment formed after 6% fractional melting of DMM mantle (Table S6). **a** Mass (g) of the assimilated and fractionated phases, on the basis of 100 grams of melt; **b** Modal proportion (vol%) of the assimilated and fractionated phases

The clinopyroxene and orthopyroxene compositions (Table S6) computed after 20% fractionation of the melt at 1335 °C (Fig. 9) fit the areal analyses of porphyroclastic clinopyroxene and orthopyroxene analysed in the Mt. Maggiore pyroxenites (Tables S1, S2). Spot analyses of clinopyroxene porphyroclastic cores (Fig. 9c, d; Table S1) show lower MgO and FeO concentrations and higher CaO contents as a result of extensive orthopyroxene exsolution, and therefore are not reproduced by the model. We emphasize the importance of the use of areal analyses of the porphyroclastic pyroxene cores to reconstruct their primary composition (Fig. S1). Yet, discrepancies are observed between the areal analyses and the computed Al_2O_3 concentrations in orthopyroxene, which is overestimated by pMELTS modeling (Fig. 9e). It is worth noting that pMELTS thermodynamic models (Ghiorso et al. 2002) do not integrate Cr_2O_3 in pyroxenes and given the high Cr_2O_3 concentration in porphyroclastic orthopyroxenes (Fig. 4d), a substitution of Cr_2O_3 by Al_2O_3 in the modeled orthopyroxene M1 site would lead to a large computational error. Our modeling thus shows that the Mt. Maggiore pyroxenites correspond in terms of modal and chemical compositions (Figs. 8, 9) to spinel websterites formed by reactive fractional crystallization after 20% fractionation of depleted melts at 1335 °C.

Spinel-facies reactive porous flow

To simulate the reactive porous flow process occurring at spinel-facies, leading to partial dissolution of pyroxene porphyroclasts and crystallization of interstitial olivine (Fig. 2a, b) we performed a model of reactive fractional crystallization from 8 kbar to 7 kbar, at temperatures decreasing from 1320 to 1290 °C. We used as initial melt composition the computed melt after formation of the pyroxenite at 1335 °C in the previous model (Table 3). Based on microstructural constraints (Fig. 2a, b), this model assumes the assimilation of 0.1 g/ °C of porphyroclastic pyroxenes (75% orthopyroxene, 25% clinopyroxene). The melt reactivity is related to the expansion of the olivine stability field at decreasing pressure (Kelemen et al. 2007).

Figure 10 shows the modal composition of the products and assimilated phases of the reactive porous flow process. While temperature decreases from 1320 to 1290 °C, the percolating melt assimilates a total of 3 g of pyroxenes (2.25 g orthopyroxene, 0.75 g clinopyroxene) and fractionates 4.5 g of olivine (Fig. 10a; Table S6). This implies a rather high Ma/Mc of ~ 0.6–0.7 (Fig. 10b) and an almost constant liquid mass during the reactive porous flow process (Table S6),

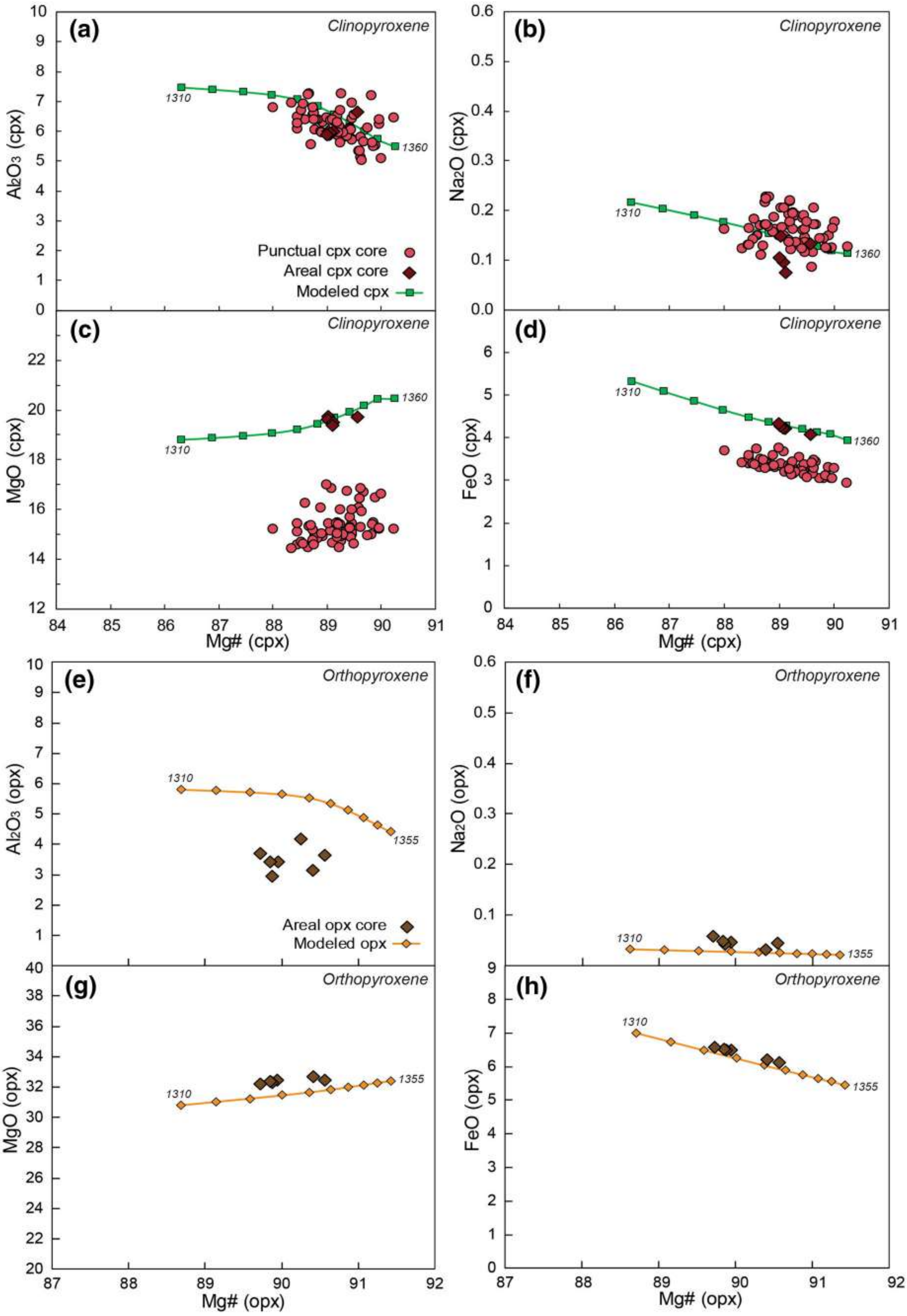
(a)
Clinopyroxene
Al2O3 (cpx)
1310
1360
Punctual cpx core
Areal cpx core
Modeled cpx
(b)
Clinopyroxene
Na2O (cpx)
1310
1360
(c)
Clinopyroxene
MgO (cpx)
1310
1360
(d)
Clinopyroxene
FeO (cpx)
1310
1360
Mg# (cpx)
84 85 86 87 88 89 90 91
(e)
Orthopyroxene
Al2O3 (opx)
1310
1355
Areal opx core
Modeled opx
(f)
Orthopyroxene
Na2O (opx)
1310
1355
(g)
Orthopyroxene
MgO (opx)
1310
1355
(h)
Orthopyroxene
FeO (opx)
1310
1355
Mg# (opx)
87 88 89 90 91 92

◂**Fig. 9** Mg# (mol%) vs Major element concentrations of clinopyroxenes (**a**–**d**) and orthopyroxenes (**e**–**h**) analysed in Mt. Maggiore pyroxenites and modeled by the pMELTS reactive fractional crystallization process. **a**, **e** Al_2O_3 (wt%); **b**, **f** Na_2O (wt%); **c**, **g** MgO (wt%); **d**, **h** FeO (wt%). Numbers associated with the crystallization trends correspond to crystallization temperatures

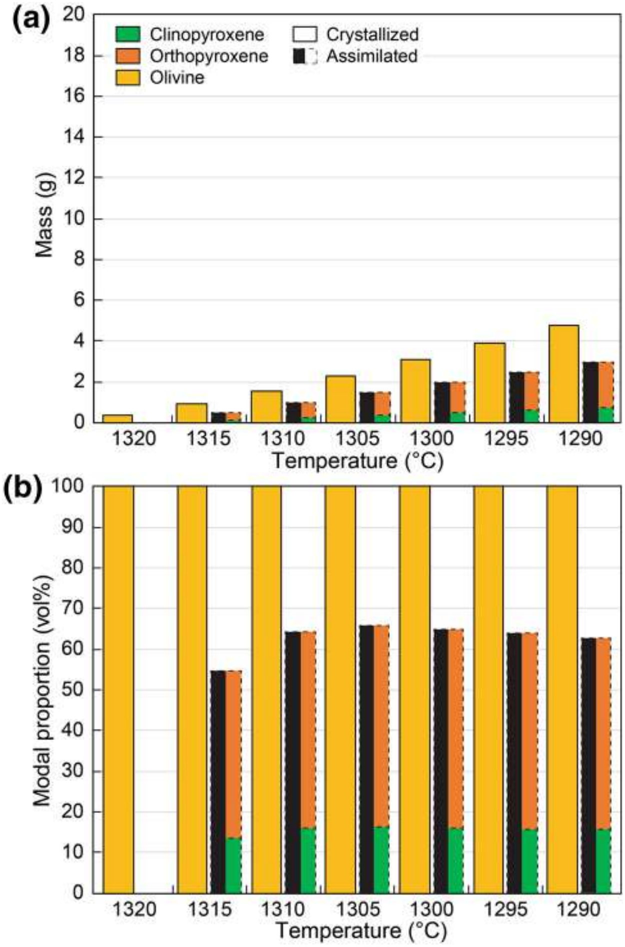

Fig. 10 Temperature (°C) vs cumulated modal composition of the assimilated and fractionated phases during the pMELTS model of reactive porous flow from 8 kbar, 1320 °C to 7 kbar, 1290 °C. Initial melt composition used is the 1335 °C melt output from the previous model of reactive fractional crystallization (Table S6). **a** Mass (g) of the assimilated and fractionated phases, on the basis of 100 g of melt; **b** MODAL proportion (vol%) of the assimilated and fractionated phases

consistent with what was described in previous studies (Rampone et al. 2008; Basch et al. 2018). The low amount of assimilation and fractionation of the melt along the process (Fig. 10a) is also consistent with the microstructural evidence of a reactive porous flow process integrated over time (Basch et al. 2018), i.e. each single portion of melt percolating through the matrix leads to only part of the dissolution–precipitation process observed in the pyroxenite and peridotite. The composition of the olivine fractionated from the melt is almost constant during the modeled process (Fo = 89.5–90.0 mol%; Table S6) and corresponds to the composition of olivines analysed in the pyroxenites and peridotites at Mt. Maggiore (Table S4; Rampone et al. 1997, 2008; Müntener and Piccardo 2003; Piccardo and Guarnieri 2010; Basch et al. 2018).

We attempted to perform this pMELTS thermodynamic model using as initial melt composition the 6% depleted single-melt increment (Table 3), without considering the previous stage of high-pressure segregation of the pyroxenite layers. The results of this model are shown in Figure S3 and indicate the saturation of clinopyroxene at 1305 °C, and therefore the formation of a wehrlite at decreasing temperatures (70 vol% clinopyroxene, 30 vol% olivine at 1285 °C; Fig. S4b). This does not correspond to the microstructural observations of partial dissolution of pyroxenes and crystallization of interstitial olivine related to reactive porous flow (Fig. 2a, b). This implies that the early stage of fractionation of the pyroxenite layers at high pressure is necessary to decrease the pyroxene saturation in the melt during its decompressional evolution.

Previous studies of the melt–rock interaction history at Mt. Maggiore investigated the REE evolution of depleted melts during the processes of spinel-facies reactive porous flow and melt impregnation (Rampone et al. 2008; Piccardo and Guarnieri 2010; Basch et al. 2018). However, these studies did not consider the early fractionation of pyroxenites in the melt REE evolution. We performed a simple Assimilation-Fractional Crystallization (AFC) REE model (De Paolo 1981) of the high-pressure formation of pyroxenite layers, to assess its impact on the initial depleted melt REE composition. We assume 20% fractionation of the depleted melt (melt REE composition after Basch et al. 2018), during assimilation of the country lherzolite at Ma/Mc = 0.2 (mineral compositions after Basch et al. 2018). Figure S4 shows that pyroxenite segregation does not lead to significant modification in the REE composition of the percolating melt (Ce_N/Yb_N from 0.16 to 0.17; Yb_N from 15.7 to 17.2 times C1). Therefore, the early formation of pyroxenites does not affect the previously described REE trace element evolution during reactive porous flow and impregnation processes (Basch et al. 2018).

Plagioclase-facies melt impregnation

We simulated the melt impregnation stage documented in the peridotites and pyroxenites assuming a stage of melt reactive fractional crystallization from 7 kbar, 1280 °C to 6 kbar, 1200 °C. These conditions are consistent with our geothermobarometric estimates of the impregnation process (Table 2), indicating temperatures up to 1290 °C,

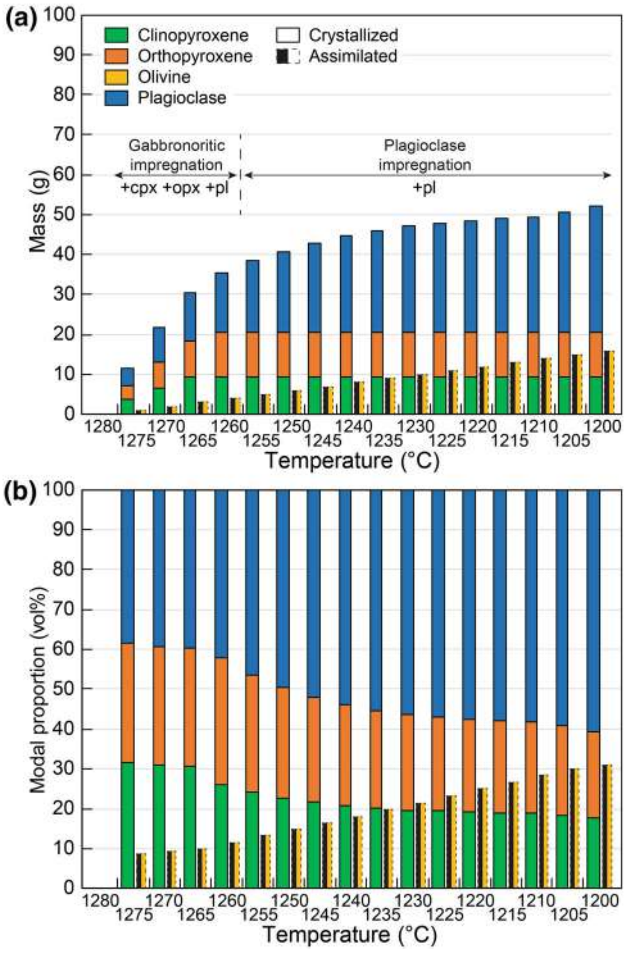

Fig. 11 Temperature (°C) vs cumulated modal composition of the assimilated and fractionated phases during the pMELTS model of melt impregnation from 7 kbar, 1280 °C to 6 kbar, 1200 °C. Initial melt composition used is the 1290 °C melt output from the previous model of reactive porous flow (Table S6). **a** Mass (g) of the assimilated and fractionated phases, on the basis of 100 g of melt; **b** modal proportion (vol%) of the assimilated and fractionated phases

at pressures of 6.4–6.6 kbar. We used as initial melt composition the computed melt after the previous model of reactive porous flow at 1290 °C (Table 3). Based on microstructural constraints (Fig. 2c, d), this model assumes the assimilation of 0.2 g/ °C of cooling of interstitial olivine Fo_{90}.

Figure 11 represents the modal composition of the products and assimilated phases during the melt impregnation model. The latter leads to an extensive crystallization of a gabbronoritic assemblage at first (plagioclase, orthopyroxene, clinopyroxene, ~ 10 g/5 °C until 1260 °C; Fig. 11a) and is then dominated by the crystallization of plagioclase alone (< 1260 °C; Fig. 11a). The gabbronoritic modal composition of the high-temperature impregnation products (Fig. 11b) is consistent with the [plagioclase + orthopyroxene ± clinopyroxene] character of the impregnation (Fig. 2c, d) and the occurrence of gabbronoritic veinlets within the most impregnated peridotites and pyroxenites (Basch et al. 2018). Ma/Mc is low (~ 0.1 to 0.3; Fig. 11b), implying that the melt mass and porosity decrease rapidly during the impregnation process, consistently with what was described in previous studies (Rampone et al. 2008; Basch et al. 2018).

Fig. 12 Major element concentrations of orthopyroxenes (Mg# vs **a**–**d**) and plagioclase (SiO_2 vs **e**–**h**) analysed in Mt. Maggiore pyroxenites and modeled by the pMELTS melt impregnation process. **a** Al_2O_3 (wt%); **b** Na_2O (wt%); **c** MgO (wt%); **d** FeO (wt%); **e** An (mol%); **f** Na_2O (wt%); **g** Al_2O_3 (wt%); CaO (wt%). Numbers associated with the crystallization trends correspond to crystallization temperatures ▸

The major element compositions of interstitial plagioclase and orthopyroxene analysed in the pyroxenites (Tables S2, S3) fit well to the compositions of plagioclase and orthopyroxene fractionated from the melt at 1270–1280 °C in the pMELTS model (Fig. 12). Again, the largest discrepancy between the measured and computed mineral compositions is the Al_2O_3 content in orthopyroxene (Fig. 12a). We infer that this mismatch is due to a pMELTS computational error as previously discussed (see "High-pressure segregation of the pyroxenite layers"). This model therefore reproduces the microstructural observations related to the stage of melt impregnation (Fig. 11) and the geochemical composition of the mineral phases (plagioclase, orthopyroxene, clinopyroxene) as products of melt impregnation at 1270–1280 °C (Fig. 12).

Depleted melts in slow-spreading oceanic environments

Melt migration in a thick thermal boundary layer

The peridotites from Mt. Maggiore have been previously described as one of the few occurrences of oceanic mantle in the Alpine-Apennine ophiolites (e.g. Rampone et al. 2019). They record a multi-stage history of decompressional melting and subsequent melt–rock interactions, related to the opening of the ultra-slow-spreading Ligurian Tethys basin (Fig. 13a). In this oceanic context, the pMELTS thermodynamic models developed in this study allowed to reconstruct the pressure–temperature evolution (Fig. S5), ranging from adiabatic decompression to conductive cooling in the oceanic lithosphere. The thermodynamic models define a cold thermal regime (Fig. S5), in which decompressional melting of the peridotite occurs over a restricted range of pressure (13.6–10 kbar), and stops at relatively high pressures (10 kbar ~ 30 km) while being incorporated into the TBL (Fig. S6; e.g. Langmuir and Forsyth 2007). In this thick TBL, high-temperature magmatic processes are followed by plagioclase-facies sub-solidus reequilibration documented in the

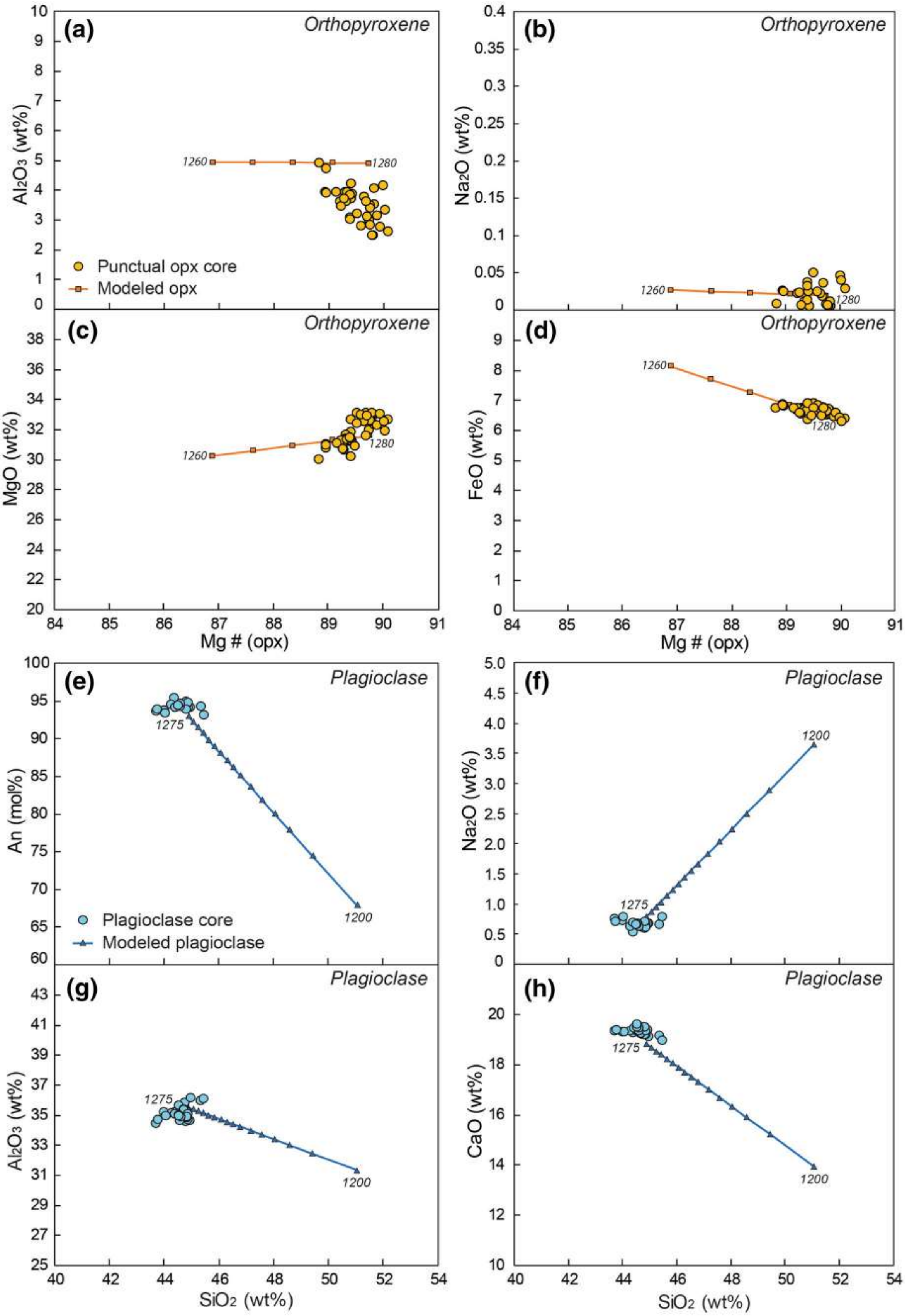
(a)
Orthopyroxene
Al2O3 (wt%)
1260
1280
Punctual opx core
Modeled opx
(b)
Orthopyroxene
Na2O (wt%)
1260
1280
(c)
Orthopyroxene
MgO (wt%)
1260
1280
Mg # (opx)
(d)
Orthopyroxene
FeO (wt%)
1260
1280
Mg # (opx)
(e)
Plagioclase
An (mol%)
1275
1200
Plagioclase core
Modeled plagioclase
(f)
Plagioclase
Na2O (wt%)
1275
1200
(g)
Plagioclase
Al2O3 (wt%)
1275
1200
SiO2 (wt%)
(h)
Plagioclase
CaO (wt%)
1275
1200
SiO2 (wt%)

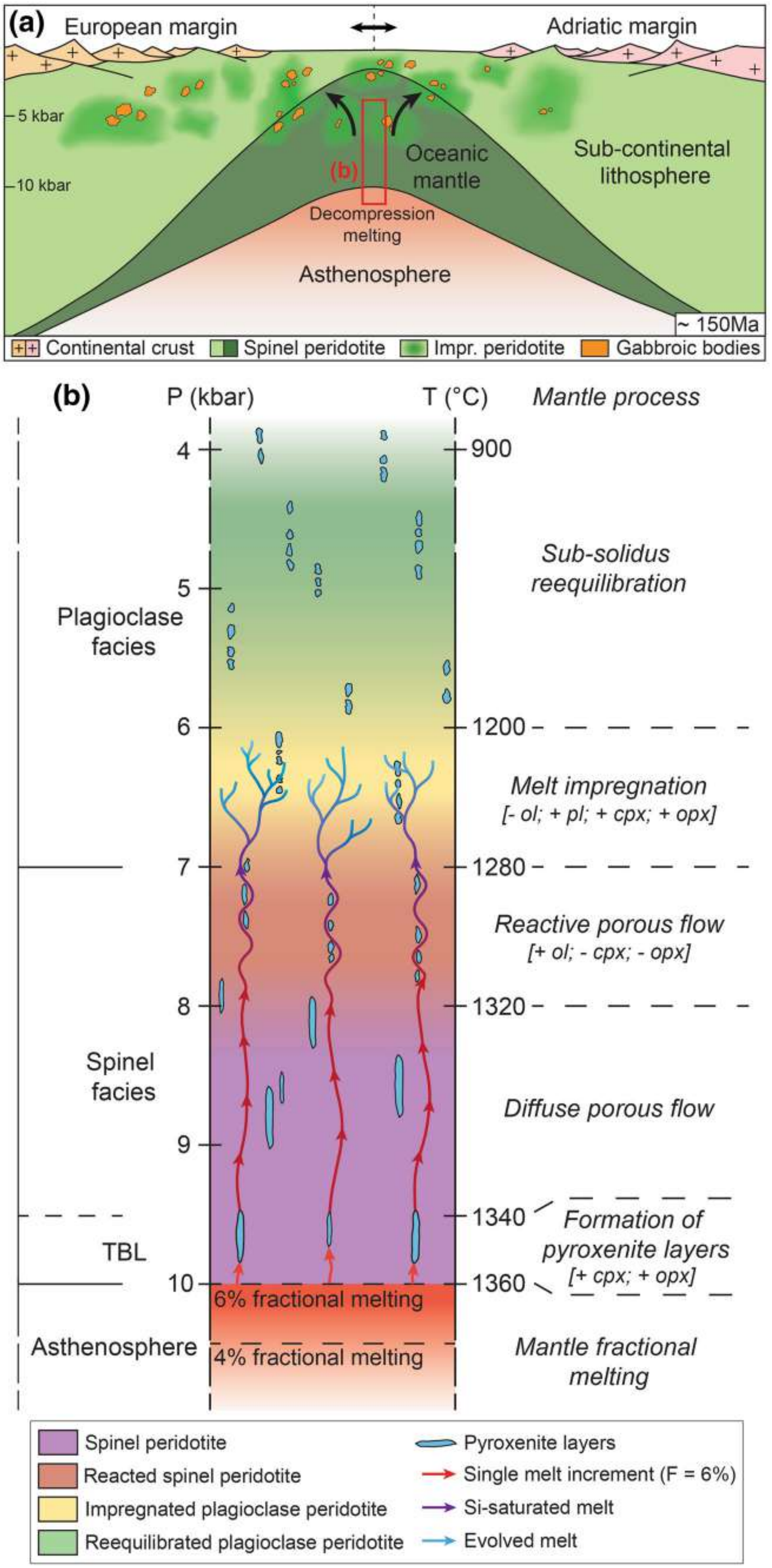
(a)
European margin
Adriatic margin
5 kbar
10 kbar
(b)
Oceanic mantle
Sub-continental lithosphere
Decompression melting
Asthenosphere
~ 150Ma
Continental crust
Spinel peridotite
Impr. peridotite
Gabbroic bodies
(b)
P (kbar)
T (°C)
Mantle process
4
5
6
7
8
9
10
900
1200
1280
1320
1340
1360
Plagioclase facies
Spinel facies
TBL
Asthenosphere
Sub-solidus reequilibration
Melt impregnation
[- ol; + pl; + cpx; + opx]
Reactive porous flow
[+ ol; - cpx; - opx]
Diffuse porous flow
Formation of pyroxenite layers
[+ cpx; + opx]
Mantle fractional melting
6% fractional melting
4% fractional melting
Spinel peridotite
Reacted spinel peridotite
Impregnated plagioclase peridotite
Reequilibrated plagioclase peridotite
Pyroxenite layers
Single melt increment (F = 6%)
Si-saturated melt
Evolved melt

Fig. 13 Interpretative sketches of the geological context of the Mt. Maggiore peridotitic body. **a** Context of formation of the pyroxenite layers and melt percolation through a thick lithosphere in the Jurassic Ligurian Tethys basin; **b** mantle column representing the different modeled stages (from mantle melting to spinel-facies reactive percolation to plagioclase-facies melt impregnation; see detail in the text)

plagioclase-bearing assemblage within the peridotites and associated pyroxenites (780–1080 °C, 3–5 kbar; Table 2). Thick TBL have been described in slow-spreading ophiolitic (Müntener et al. 2010; Sanfilippo et al. 2017; Rampone et al. 2019; Basch et al. 2019) and oceanic environments (Langmuir et al. 1992; Cannat 1996; Niu 1997; Kelemen et al. 2007; Langmuir and Forsyth 2007; Montési and Behn 2007; Dick et al. 2010; Hebert and Montési 2010; Warren and Shimizu 2010; Sleep and Warren 2014; D'Errico et al. 2016), consistent with the geodynamic context of the Mt. Maggiore peridotitic body and Ligurian Tethys basin (Fig. 13a). Deep conductive cooling in slow-spreading lithosphere favours the freezing of melts percolating in the shallow mantle.

Hebert and Montési (2010) modeled the depth of the crystallization front as a function of spreading rate at mid-ocean ridges. The crystallization front corresponds to the depth at which migrating melts experience extensive crystallization at the double saturation of plagioclase and clinopyroxene. At spreading rates comparable to those estimated for the Ligurian Tethys basin (20 mm/year full spreading rate; see Rampone et al. 2014 and cited references), their model predicts the depth of the crystallization front at 18 km (~ 6 kbar). This is consistent with our pMELTS models indicating double saturation of plagioclase and clinopyroxene and extensive crystallization rates at 7 kbar (Fig. 11; see "Plagioclase-facies melt impregnation"). Therefore, the pMELTS thermodynamic models developed in this study are in good agreement with the typical thermal architecture (Fig. S5) expected for a cold ultra-slow-spreading environment (Fig. 13a).

Continuous evolution of depleted melts in a mantle column

The thermodynamic models evidence the continuity of the described processes and therefore a continuous evolution of the depleted initial melt composition, from the formation of the pyroxenite layers to the reactive porous flow and impregnation processes (Fig. S5). The major element pMELTS modeling demonstrated the necessity of including the early fractionation of pyroxenes in the melt evolution, leading to a decrease of pyroxene saturation in the melt (see "Spinel-facies reactive porous flow; Fig. S4). This decreased saturation is crucial to model the following spinel-facies reactive porous flow process without reaching saturation of clinopyroxene (Fig. S4) and, therefore, to reproduce the microstructural observations of a pyroxene-dissolving, olivine-crystallizing reactive porous flow.

The continuity of these reactive processes occurring at different depths in the conductive lithosphere (Fig. S5) also implies a vertical evolution of the types of melt–rock interactions (Rampone et al. 2019). Therefore, all processes occur at the same time at different depths in a mantle column in exhumation (Fig. 13b). To form the microstructural assemblages observed in our samples (impregnated pyroxenite reequilibrated to sub-solidus plagioclase-facies conditions), a pyroxenite layer formed at 10 kbar needs to reach the pressure–temperature conditions that account for extensive sub-solidus reequilibration (800 °C, 3 kbar; Table 3). The full spreading rate of the Ligurian Tethys has been estimated to be 20 mm/year (Rampone et al. 2014), which, following the equations of McKenzie (1969) and Warren et al. (2009), corresponds to an exhumation rate of 12.7 mm/year. At this rate, a pyroxenite layer formed at relatively high pressure (10 kbar–30 km) would be exhumed to shallow depths (3 kbar–9 km) in 1.6 Ma (Fig. 13b). Their formation and subsequent impregnation by depleted melts imply that generation of these melts is a continuous process characterized by steady-state isotherms over the estimated duration of mantle exhumation. Our models demonstrate that a single process of mantle adiabatic decompression governs the formation of depleted melts. Percolation of such depleted melts in turn drive all the documented reactive processes occurring in the thick oceanic lithosphere.

Pyroxenites at ultra-slow-spreading ridges

The Mt. Maggiore pyroxenites, similar to what was documented for abyssal pyroxenites from the South-West Indian Ridge and Gakkel Ridge, originated as deep melt segregations from depleted melts (Dantas et al. 2007; Laukert et al. 2014). Our modeling shows that the same depleted melts subsequently percolated this mantle sector, originating reactive harzburgites and dunites (at spinel-facies depth) and impregnated peridotites (at plagioclase-facies depth) during progressive upward migration. As discussed by Rampone et al. (2019), we thus infer that the depleted signature of these melts is a primary feature, reflecting their origin as single depleted melt increments. Depleted melts are presently documented in oceanic and ophiolitic peridotites from ultra-slow-spreading environments only (e.g., South-West Indian Ridge, Dantas et al. 2007; Othris peridotites, Dijkstra et al. 2003; Lanzo peridotites, Piccardo et al. 2007; Mt. Maggiore peridotites, Piccardo and Guarnieri 2010; Basch et al. 2018). At such settings, low melt production and thick TBL may favour the preservation of unaggregated last depleted melt increments formed at the top of an upwelling melting mantle column.

Our models demonstrate that the expansion of olivine stability field during upward migration of the depleted melts does not account alone for the spinel-facies reactive porous flow leading to dissolution of mantle pyroxenes (see "Spinel-facies reactive porous flow"). Thus, the early segregation of pyroxenitic components is a necessary process in lowering the pyroxene saturation in the migrating melt and could be fundamental in the formation of olivine-saturated pyroxene-undersaturated melts. Migration of unaggregated melts and high-pressure crystallization of pyroxenites are favoured in a thick TBL and are likely to be a common feature at ultra-slow spreading ridges, such as the South-West Indian Ridge and Lena Trough (Dantas et al. 2007; Laukert et al. 2014).

Summary and conclusions

This study investigates the formation of the pyroxenite layers associated with the residual peridotites of the Mt. Maggiore. Combined microstructural and geochemical analyses point to a magmatic formation of the pyroxenite, as part of the complex reactive percolation history of depleted single-melt increments. We performed pMELTS models of this evolution as follows:

1. Formation of the depleted melts by fractional melting of a DMM in an ultra-slow-spreading environment, in which the thick TBL terminates the melting process at rather high pressure (10 kbar);
2. Reactive crystallization of the pyroxenite layers (75% clinopyroxene, 20% orthopyroxene, 5% spinel) during fractionation of the depleted melt at depth (Mc = 20%), and assuming the assimilation of small quantities of host peridotite (Ma/Mc = 0.2).
3. Spinel-facies reactive porous flow of the modified melt leads to the assimilation of pyroxenes and crystallization of interstitial olivine, without significant modification in the melt mass (Ma/Mc = 0.6–0.7; Mc < 5%).
4. The percolation of the modified depleted melts at shallower levels leads to the crystallization of gabbronoritic assemblages (plagioclase, orthopyroxene, clinopyroxene) at the expense of olivine (Ma/Mc = 0.1–0.2) during impregnation of the peridotites and associated pyroxenites.

The formation of pyroxenite layers from unaggregated depleted melts in ultra-slow spreading environments testifies their importance in the geochemical evolution of the melt percolating in the oceanic lithosphere. The early fractionation of pyroxenites leads to a decrease in pyroxene saturation, in turn favouring the subsequent reactive porous flow process leading to the dissolution of mantle pyroxenes at spinel-facies.

Acknowledgements We thank Veronique Le Roux and an anonymous reviewer for constructive reviews that improved the quality of this manuscript and O. Müntener for his work as editor. We thank Paolo Campanella and Alessandra Gavoglio, Christophe Nevado and Doriane Delmas for realization of the thin section and high-quality polishing, as well as Fabrice Barou for assistance with the EBSD analyses, Andrea Risplendente for assistance with the EPMA. This research has been supported by the Italian Ministry of Education, University and Research (MIUR) through the grant [PRIN-2015C5LN35] "Melt–rock reaction and melt migration in the MORB mantle through combined natural and experimental studies".

References

Allègre CJ, Turcotte DL (1986) Implications of a two-component marble-cake mantle. Nature 323:123–127

Basch V (2018) Melt–rock interactions in the oceanic lithosphere: microstructural and petro-geochemical constraints from ophiolites. Ph.D. thesis, Università degli Studi di Genova. https://doi.org/10.15167/basch-valentin_phd2018-05-10

Basch V, Rampone E, Crispini L, Ferrando C, Ildefonse B, Godard M (2018) From mantle peridotites to hybrid troctolites: textural and chemical evolution during melt–rock interaction history (Mt. Maggiore, Corsica, France). Lithos 323:4–23. https://doi.org/10.1016/j.lithos.2018.02.025

Basch V, Rampone E, Crispini L, Ferrando C, Ildefonse B, Godard M (2019) Multi-stage reactive formation of troctolites in slow-spreading oceanic lithosphere (Erro-Tobbio, Italy): a combined field and petrochemical study. J Petrol. https://doi.org/10.1093/petrology/egz019

Ben Ismail W, Barruol G, Mainprice D (2001) The Kaapvaal craton seismic anisotropy: petrophysical analyses of upper mantle kimberlite nodules. Geophys Res Lett 28:2497–2500. https://doi.org/10.1029/2000GL012419

Bodinier J-L, Fabries J, Lorand J-P, Dostal J, Dupuy C (1987a) Geochemistry of amphibole pyroxenite veins from the Lherz and Freychinede ultramafic bodies (Ariege, French Pyrenees). Bull Minér 110:345–358

Bodinier J-L, Guiraud M, Fabries J, Dostal J, Dupuy C (1987b) Petrogenesis of layered pyroxenites from the Lherz, Freychinede and Prades ultramafic bodies (Ariege, French Pyrenees). Geochim Cosmochim Acta 51:279–290

Bodinier J-L, Garrido CJ, Chanefo I, Bruguier O, Gervilla F (2008) Origin of pyroxenite–peridotite veined mantle by refertilization reactions: evidence from the Ronda peridotite (Southern Spain). J Petrol 49:999–1025

Borghini G, Fumagalli P, Rampone E (2010) The stability of plagioclase in the upper mantle: subsolidus experiments on fertile and depleted lherzolite. J Petrol 51:229–254

Borghini G, Fumagalli P, Rampone E (2011) The geobarometric significance of plagioclase in mantle peridotites: a link between nature and experiments. Lithos 126:42–53

Borghini G, Rampone E, Zanetti A, Class C, Cipriani A, Hofmann AW, Goldstein SL (2013) Meter-scale Nd isotopic heterogeneity in pyroxenite-bearing Ligurian peridotites encompasses global-scale upper mantle variability. Geology 41:1055–1058

Borghini G, Rampone E, Zanetti A, Class C, Cipriani A, Hofmann AW, Goldstein SL (2016) Pyroxenite layers in the Northern Apennines' Upper Mantle (Italy)—generation by pyroxenite melting and melt infiltration. J Petrol 57:625–653

Borghini G, Fumagalli P, Rampone E (2017) Partial melting of secondary pyroxenite at 1 and 15 GPa, and its role in upwelling heterogeneous mantle. Contrib Mineral Petrol 172:70. https://doi.org/10.1007/s00410-017-1387-4

Borghini G, Francomme JE, Fumagalli P (2018) Melt–dunite interactions at 0.5 and 0.7 GPa: experimental constraints on the origin of olivine-rich troctolites. Lithos 323:44–57

Brey GP, Köhler T (1990) Geothermobarometry in four phase lherzolites II. New thermobarometers, and practical assessment of existing thermobarometers. J Petrol 31:1353–1378

Cannat M (1996) How thick is the magmatic crust at slow spreading ridges? J Geophys Res Solid Earth 101:2847–2857

Collier ML, Kelemen PB (2010) The case for reactive crystallization at Mid-Ocean ridges. J Petrol 51:1913–1940. https://doi.org/10.1093/petrology/egq043

Dantas C, Ceuleneer G, Gregoire M, Python M, Freydier R, Warren J, Dick HJB (2007) Pyroxenites from the Southwest Indian Ridge, 9°–16°E: cumulates from incremental melt fraction produced at the top of a cold melting regime. J Petrol 48:647–660

Dantas C, Gregoire M, Koester E, Conceicao RD, Rieck N (2009) The lherzolite–websterite xenolith suite from Northern Patagonia (Argentina): evidence of mantle–melt reaction processes. Lithos 107:107–120

De Paolo DJ (1981) Trace elements and isotopic effects of combined wall rock assimilation and fractional crystallization. Earth Planet Sci Lett 53:189–202

D'Errico ME, Warren JM, Godard M (2016) Evidence for chemically heterogeneous Arctic mantle beneath the Gakkel ridge. Geochim Cosmochim Acta 174:291–312. https://doi.org/10.1016/j.gca.2015.11.017

Dick HJB, Lissenberg CJ, Warren JM (2010) Mantle melting melt transport, and delivery beneath a slow-spreading ridge: the paleo-MAR from 23°15′N to 23°45′N. J Petrol 51:425–467. https://doi.org/10.1093/petrology/egp088

Dijkstra AH, Barth MG, Drury MR, Mason PRD, Vissers RLM (2003) Diffuse porous melt flow and melt-rock reaction in the mantle lithosphere at a slow-spreading ridge: a structural petrology and LA-ICP-MS study of the Othris peridotite massif (Greece). Geochem Geophys Geosyst 4:8613. https://doi.org/10.1029/2001GC000278

Duncan RA, Green DH (1980) The role of multi-stage melting in the formation of the oceanic crust. Geology 8:22–26

Duncan RA, Green DH (1987) The genesis of refractory melts in the formation of oceanic crust. Contrib Miner Petrol 96:326–342

Falloon TJ, Green DH (1988) Anhydrous partial melting of peridotite from 8 to 35 kbars and the petrogenesis of MORB. J Petrol 1:379–414

Ferrando C, Godard M, Ildefonse B, Rampone E (2018) Melt transport and mantle assimilation at Atlantis Massif (IODP Site U1309): constraints from geochemical modelling. Lithos 323:24–43

Fumagalli P, Borghini G, Rampone E, Poli S (2017) Experimental calibration of Forsterite–Anorthite–Ca-Tschermak-Enstatite (FACE) geobarometer for mantle peridotites. Contrib Miner Petrol 172:38

Garrido CJ, Bodinier JL (1999) Diversity of mafic rocks in the Ronda peridotite: evidence for pervasive melt– rock reaction during heating of subcontinental lithosphere by upwelling asthenosphere. J Petrol 40:729–754

Ghiorso MS, Hirschmann M, Reiners PW, Kress VCI (2002) The pMELTS: a revision of MELTS aimed at improving calculation of phase relations and major element partitioning involved in partial melting of the mantle at pressures up to 3 GPa. Geochem Geophys Geosyst 3:36

Gysi AP, Jagoutz O, Schmidt MW, Targuisti K (2011) Petrogenesis of pyroxenites and melt infiltrations in the ultramafic complex of Beni Bousera, Northern Morocco. J Petrol 52:1676–1735

Hebert LB, Montési LGJ (2010) Generation of permeability barriers during melt extraction at mid-ocean ridges. Geochem Geophys Geosyst 11:Q12008. https://doi.org/10.1029/2010GC003270

Higgie K, Tommasi A (2012) Feedbacks between deformation and melt distribution in the crust-mantle transition zone of the Oman ophiolite. Earth Planet Sci Lett 359–360:61–72. https://doi.org/10.1016/j.epsl.2012.10.003

Higgie K, Tommasi A (2014) Deformation in a partially molten mantle: constraints from plagioclase lherzolites from Lanzo, western Alps. Tectonophysics 615–616:167–181. https://doi.org/10.1016/j.tecto.2014.01.007

Hirose K, Kushiro I (1993) Partial melting of dry peridotites at high pressures: determination of compositions of melts segregated from peridotite using aggregates of diamond. Earth Planet Sci Lett 114:477–489

Hirschmann MM, Stolper EM (1996) A possible role for garnet pyroxenite in the origin of the "garnet signature" in MORB. Contrib Miner Petrol 124:185–208

Holtzman BK, Kohlstedt DL, Zimmerman ME, Heidelbach F, Hiraga T, Hustoft J (2003) Melt segregation and strain partitioning: implications for seismic anisotropy and mantle flow. Science 301:1227–1230. https://doi.org/10.1126/science.1087132

Husen A, Renat RA, Holtz F (2016) The effect of H2O and pressure on multiple saturation and liquid lines of descent in basalt from the Shatsky rise. J Petrol 57:309–344. https://doi.org/10.1093/petrology/egw008

Jackson MD, Ohnenstetter M (1981) Peridotite and gabbroic structures in the Monte Maggiore massif, Alpine Corsica. J Geol 89:703–719

Johnson KTM, Dick HJB, Shimizu N (1990) Melting in the oceanic upper mantle: an ion microprobe study of diopsides in abyssal peridotites. J Geophys Res 95:2661–2678. https://doi.org/10.1029/JB095iB03p02661

Kaczmarek MA, Tommasi A (2011) Anatomy of an extensional shear zone in the mantle, Lanzo massif, Italy. Geochem Geophys Geosyst 12:Q0AG06. https://doi.org/10.1029/2011GC003627

Kelemen PB, Kikawa E, Miller DJ, Shipboard Scientific Party (2007) Leg 209 summary: processes in a 20-km thick conductive boundary layer beneath the Mid-Atlantic Ridge, 14°–16°N. In: Kelemen PB, Kikawa E, Miller DJ (eds) Proceedings of the ocean drilling project, scientific results vol 209. Ocean Drilling Program, College Station, pp 1–33. https://doi.org/10.2973/odp.proc.sr.209.001.2007

Kempton PD, Stephens CJ (1997) Petrology and geochemistry of nodular websterites inclusions in harzburgite, Hole 920D. In: Karson JA et al (eds) Proceedings of the Ocean drilling program, scientific results, vol 153. Ocean Drilling Program, College Station, pp 321–331

Keshav S, Sen G, Presnall DC (2007) Garnet-bearing xenoliths from Salt Lake Crater, Oahu, Hawaii: high-pressure fractional crystallization in the oceanic mantle. J Petrol 48:1681–1724

Kinzler RJ, Grove TL (1992) Primary magmas of mid-ocean ridge basalts 1. Experiments and methods. J Geophys Res 97:6907–6926

Kogiso T, Hirschmann MM, Pertermann M (2004a) High pressure partial melting of mafic lithologies in the mantle. J Petrol 45:2407–2422

Kogiso T, Hirschmann MM, Reiners W (2004b) Length scales of mantle heterogeneities and their relationship to ocean island basalt geochemistry. Geochim Cosmochim Acta 68:345–360

Lambart S, Laporte D, Schiano P (2013) Markers of the pyroxenite contribution in the major-element compositions of oceanic basalts: review of the experimental constraints. Lithos 160–161:14–36

Lambart S, Baker MB, Stolper EM (2016) The role of pyroxenite in basalt genesis: Melt-PX, a melting parameterization for mantle pyroxenites between 0.9 and 5 GPa. J Geophys Res Solid Earth 121:5708–5735

Langmuir CH, Forsyth DW (2007) Mantle melting beneath mid-ocean ridges. Oceanography 20:78–89

Langmuir CH, Klein EM, Plank T (1992) Petrological systematics of mid-ocean ridge basalts: Constraints on melt generation beneath ocean ridges. In: Phipps Morgan J, Blackman DK, Sinton JM (eds) Mantle flow and melt generation at mid-ocean ridges. American Geophysical Union, Washington, DC, pp 183–280

Laukert G, Von der Handt A, Hellebrand E, Snow J, Hoppe P, Klugel A (2014) High-pressure reactive melt stagnation recorded in abyssal pyroxenites from the ultraslow-spreading Lena Trough, Arctic Ocean. J Petrol 55:427–458

Le Roux V, Tommasi A, Vauchez A (2008) Feedback between melt percolation and deformation in an exhumed lithosphere-asthenosphere boundary. Earth Planet Sci Lett 274:401–413. https://doi.org/10.1016/j.epsl.2008.07.053

Mainprice D, Bachmann F, Hielscher R, Schaeben H (2014) Descriptive tools for the analysis of texture projects with large datasets using MTEX: strength, symmetry and components. Geological Society of London, London **(Special Publication)**

McCarthy A, Muntener O (2019) Evidence for ancient fractional melting, cryptic refertilization and rapid exhumation of Tethyan mantle (Civrari Ophiolite, NW Italy). Contrib Miner Petrol 174:69–93

McKenzie DP (1969) Speculations on the consequences and causes of plate motions. Geophys J R Astron Soc 18:1–32

Montési LGJ, Behn MD (2007) Mantle flow and melting underneath oblique and ultraslow MORs. Geophys Res Lett 34:L24307

Morishita T, Arai S (2001) Petrogenesis of corundum-bearing mafic rock in the Horoman Peridotite Complex, Japan. J Petrol 42:1279–1299

Morishita T, Arai S, Gervilla F, Green DH (2003) Closed system geochemical recycling of crustal materials in the upper mantle. Geochim Cosmochim Acta 67:303–310

Mukasa SB, Shervais JW (1999) Growth of sub-continental lithosphere: evidence from repeated injections in the Balmuccia lherzolite massif, Italian Alps. Lithos 48:287–316

Müntener O, Piccardo GB (2003) Melt migration in ophiolitic peridotites: the message from Alpine-Apennine peridotites and implications for embryonic ocean basin. In: Dilek Y, Robinson PT (eds) Ophiolites in earth history, vol 218. Geological Society of London, London, pp 69–89 **(Special Publication)**

Müntener O, Manatschal G, Desmurs L, Pettke T (2010) Plagioclase peridotites in ocean-continent transitions: refertilized mantle domains generated by melt stagnation in the shallow mantle lithosphere. J Petrol 51:255–294

Niu Y (1997) Mantle melting and melt extraction processes beneath ocean ridges: evidence from abyssal peridotites. J Petrol 38:1047–1074

Niu Y, Hékinian R (1997) Spreading-rate dependence of the extent of mantle melting beneath ocean ridges. Nature 385:326–329

Paquet M, Cannat M, Brunelli D, Hamelin C, Humler E (2016) Effect of melt/mantle interactions on MORB chemistry at the easternmost southwest Indian ridge (61° to 67°E). Geochem Geophys Geosyst 17:4605–4640. https://doi.org/10.1002/2016GC006385

Piccardo GB, Guarnieri L (2010) The Monte Maggiore peridotite (Corsica, France): a case study of mantle evolution in the Ligurian Tethys. Geol Soc Lond 337:7–45. https://doi.org/10.1144/SP337.20305-8719/10

Piccardo GB, Zanetti A, Müntener O (2007) Melt-peridotite interaction in the southern Lanzo peridotite: field, textural and geochemical evidence. Lithos 94:181–209

Rampone E, Borghini G (2008) Melt migration and intrusion in the Erro-Tobbio peridotites (Ligurian Alps, Italy): insights on magmatic processes in extending lithospheric mantle. Eur J Miner 20:573–585

Rampone E, Piccardo GB, Vannucci R, Bottazzi P (1997) Chemistry and origin of trapped melts in ophiolitic peridotites. Geochim Cosmochim Acta 61:4557–4569

Rampone E, Piccardo GB, Hofmann AW (2008) Multistage melt–rock interaction in the Mt. Maggiore (Corsica, France) ophiolitic peridotites: microstructural and geochemical records. Contrib Miner Petrol 156:453–475

Rampone E, Borghini G, Romairone A, Abouchami W, Class C, Goldstein SL (2014) Sm–Nd geochronology of the Erro-Tobbio gabbros (Ligurian Alps, Italy): insights into the evolution of the Alpine Tethys. Lithos 205:236–246

Rampone E, Borghini G, Godard M, Ildefonse B, Crispini L, Fumagalli P (2016) Melt/rock reaction at oceanic peridotite/gabbro transition as revealed by trace element chemistry of olivine. Geochim Cosmochim Acta 190:308–331

Rampone E, Borghini G, Basch V (2019) Melt migration and melt–rock reaction in the Alpine-Apennine peridotites: insights on mantle dynamics in extending lithosphere. Geosci Front. https://doi.org/10.1016/j.gsf.2018.11.001

Rivalenti G, Mazzucchelli M, Vannucci R, Hofmann AW, Ottolini L, Obermiller W (1995) The relationship between websterite and peridotite in the Balmuccia peridotite massif (NW Italy) as revealed by trace element variations in clinopyroxene. Contrib Miner Petrol 121:275–288

Salters VJM, Dick HJB (2002) Mineralogy of the mid ocean ridge basalt source from neodymium isotopic composition of abyssal peridotites. Nature 418:68–72

Sanfilippo A, Tribuzio R (2011) Melt transport and deformation history in a nonvolcanic ophiolitic section, northern Apennines, Italy: implications for crustal accretion at slow-spreading settings. Geochem Geophys Geosyst 12:Q0AG04. https://doi.org/10.1029/2010GC003429

Sanfilippo A, Dick HJB, Ohara Y, Tiepolo M (2016) New insights on the origin of troctolites from the breakaway area of the Godzilla Megamullion (Parece Vela back-arc basin): the role of melt-mantle interaction on the composition of the lower crust. Island Arc 25:220–234. https://doi.org/10.1111/iar.12137

Sanfilippo A, Tribuzio R, Ottolini L, Hamada M (2017) Water, lithium and trace element compositions of olivine from Lanzo South replacive mantle dunites (Western Alps): new constraints into melt migration processes at cold thermal regimes. Geochim Cosmochim Acta 214:51–72. https://doi.org/10.1016/j.gca.2017.07.034

Seyler M, Toplis MJ, Lorand JP, Luguet A, Cannat M (2001) Clinopyroxene microtextures reveal incompletely extracted melts in abyssal peridotites. Geology 29:155–158

Shen Y, Forsyth DW (1995) Geochemical constraints on initial and final depths of melting beneath ocean ridges. J Geophys Res 100:2211–2237

Sleep NH, Warren JM (2014) Effect of latent heat of freezing on crustal generation at low spreading rates. Geochem Geophys Geosyst 15:3161–3174

Sobolev AV, Shimizu N (1993) Ultra-depleted primary melt included in an olivine from the Mid-Atlantic Ridge. Nature 363:151–154

Sobolev AV, Hofmann AW, Sobolev SV, Nikogosian IK (2005) An olivine-free mantle source of Hawaiian shield basalts. Nature 434:590–597

Sobolev AV, Hofmann AW, Kuzmin DV et al (2007) The amount of recycled crust in sources of mantle-derived melts. Science 316:412–417

Stracke A, Salters VJM, Sims KWW (1999) Assessing the presence of garnet-pyroxenite in the mantle sources of basalts through combined hafnium–neodymium–thorium isotope systematics. Geochem Geophys Geosyst 1:15

Sun S-S, McDonough WF (1989) Chemical and isotopic systematics of oceanic basalts: implications for mantle composition and processes. In: Saunders AD, Norry MJ (eds) Magmatism in the ocean basins, vol 42. Geological Society, London, pp 313–345 **(Special Publications)**

Takazawa E, Frey FA, Shimizu N, Saal N, Obata M (1999) Polybaric petrogenesis of mafic layers in the Horoman peridotite complex, Japan. J Petrol 40:1827–1831

Taylor WR (1998) An experimental test of some geothermometer and geobarometer formulations for upper mantle peridotites with application to the thermobarometry of fertile lherzolite and garnet websterite. Neues Jahrbuch für Mineral Abh 172:381–408

Tommasi A, Ishikawa A (2014) Microstructures, composition, and seismic properties of the Ontong Java Plateau mantle root. Geochem Geophys Geosyst. https://doi.org/10.1002/2014GC005452

Tommasi A, Vauchez A, Ionov DA (2008) Deformation, static recrystallization, and reactive melt transport in shallow subcontinental mantle xenoliths (Tok Cenozoic volcanic field, SE Siberia). Earth Planet Sci Lett 272:65–77. https://doi.org/10.1016/j.epsl.2008.04.020

Van Acken D, Becker H, Walker RJ, McDonough WF, Wombacher F, Ash RD, Piccoli PM (2010) Formation of pyroxenite layers in the Totalp ultramafic massif (Swiss Alps)—Insights from highly siderophile elements and Os isotopes. Geochim Cosmochim Acta 74:661–683

Vannucci R, Shimizu N, Piccardo GB, Ottolini L, Bottazzi P (1993) Distribution of trace-elements during breakdown of mantle garnet: an example from Zabargad. Contrib Miner Petrol 113:437–449

Villiger S, Ulmer P, Müntener O, Thompson B (2004) The liquid line of descent of anhydrous, mantle-derived, tholeiitic liquids by fractional and equilibrium crystallization can experimental study at 1·0 GPa. J Petrol 45:2369–2388

Villiger S, Müntener O, Ulmer P (2007) Crystallization pressures of mid-ocean ridge basalts derived from major element variations of glasses from equilibrium and fractional crystallization experiments. J Geophys Res. https://doi.org/10.1029/2006JB004342

Warren JM (2016) Global variations in abyssal peridotite compositions. Lithos 248–251:193–219. https://doi.org/10.1016/j.lithos.2015.12.023

Warren JM, Shimizu N (2010) Cryptic variations in abyssal peridotite compositions: evidence for shallow-level melt infiltration in the oceanic lithosphere. J Petrol 51:395–423. https://doi.org/10.1093/petrology/egp096

Warren JM, Shimizu N, Sakaguchi C, Dick HJB, Nakamura E (2009) An assessment of upper mantle heterogeneity based on abyssal peridotite isotopic compositions. J Geophys Res 114:B12203

Workman RK, Hart SR (2005) Major and trace element composition of the depleted MORB mantle (DMM). Earth Planet Sci Lett 231:53–72. https://doi.org/10.1016/j.epsl.2004.12.005

Yu S, Xu Y, Ma J, Zheng Y, Kuang Y, Hong L, Ge W, Tong L (2010) Remnants of oceanic lower crust in the subcontinental lithospheric mantle: trace element and Sr–Nd–O isotope evidence from aluminous garnet pyroxenite xenoliths from Jiaohe, Northeast China. Earth Planet Sci Lett 297:413–422

Publisher's Note Springer Nature remains neutral with regard to jurisdictional claims in published maps and institutional affiliations.